Seismic interpretation of Sill-Complexes in Sedimentary Basins: Implications for the Sub-Sill Imaging Problem

Christian Haug Eide[1,], Nick Schofield[2], Isabelle Lecomte[1], Simon J. Buckley[1,3] and John A. Howell[2]*

[1]*Department of Earth Science, University of Bergen, Box 7803, 5020 Bergen, Norway*

[2]*School of Geosciences,* Meston Building, *University of Aberdeen, Aberdeen, AB24 3UE, UK*

[3]*Centre for Integrated Petroleum Research, Uni Research CIPR, Box 7810, 5020 Bergen, Norway*

[*]*Correspondence:* christian.eide@uib.no

Running head: Seismic interpretation of sill-complexes

Supplementary material: A scaled version of the input panel (Fig. 5D) used for seismic modelling (A1), and very high-resolution versions of subfigures in Fig. 11 (A2-3) are available at …

Abstract

Application of 3D-seismic reflection-data to igneous systems in sedimentary basins has led to a revolution in the understanding of mafic sill-complexes. However, there is considerable uncertainty on how geometries and architecture of sill-complexes within the subsurface relates to those imaged in seismic reflection-data. To provide constraints on how sill-complexes in seismic data should be interpreted, we present synthetic seismograms generated from a seismic-scale (22x0.25 km) outcrop in East Greenland constrained by abundant field-data. This study highlights how overlying igneous rocks adversely affect imaging of underlying intrusions and rocks by decreasing seismic amplitude, frequency and making steeply dipping features near-impossible to image. Furthermore, seismic modelling in this study shows that, because of the high impedance contrast between siliciclastic host-rock and dolerites, very thin (1-5 m) intrusions should in principle be imaged in reflection-seismic data at 3 km depth. However, comparison with actual seismic data with well-data shows significant amounts of un-imaged sill intrusions, and this is likely due to limited seismic resolution, overburden complexity, inadequate velocity-models, and interference between reflections from closely spaced sills and sill-splays. Significant improvements to sill imaging and interpretation could be made by better predicting occurrence and geometry of sill intrusions and including these in velocity models.

1. Introduction

Igneous sill intrusions are common at volcanic rifted margins, in rifted basins, and in large igneous provinces (e.g. Eldholm and Coffin, 2000; Skogseid, 2001; Thomson and Hutton, 2004, Planke et al, 2005, Cartwright and Hansen, 2006; Bryan and Ferrari, 2013). Understanding the processes controlling sills in such systems is essential to improve monitoring of volcanoes (e.g. Galland, 2012), constrain magma-propagation in the crust and to volcanoes (e.g. Cartwright and Hansen, 2006a; Magee et al., 2013; 2016; Muirhead et al., 2016), and to investigate hydrocarbon systems and plan hydrocarbon exploration in intruded basins (e.g. Rateau et al 2013; Schofield et al., 2015, 2016, 2017; Millett et al., 2016; Senger et al., 2017). Because of the high density- and velocity-contrasts between mafic intrusions and sedimentary host-rock, intrusions are in principle readily imaged within seismic reflection datasets (e.g. Smallwood and Maresh, 2002). Models and understanding of igneous systems in sedimentary basins have seen significant progress following the application of 3D seismic data to study sill intrusions (e.g. Cartwright and Huuse, 2005; Thomson and Hutton, 2004; Hansen and Cartwright, 2006a; Thomson and Schofield, 2008, Schofield et al. 2012b; Magee et al., 2013; Jackson et al., 2013; Jerram and Bryan, 2015; Schofield et al. 2015). As hydrocarbon exploration moves into increasingly challenging basins, and as oil and gas fields are being targeted and discovered in the vicinity of intrusions (e.g. Tormore; Schofield et al., 2015), it is essential to have a good understanding of how real geometries of intrusions are imaged in the subsurface. In this contribution, we use field data from a large outcrop in east Greenland (Figs 1, 2) to investigate imaging issues of sills in sedimentary basins.
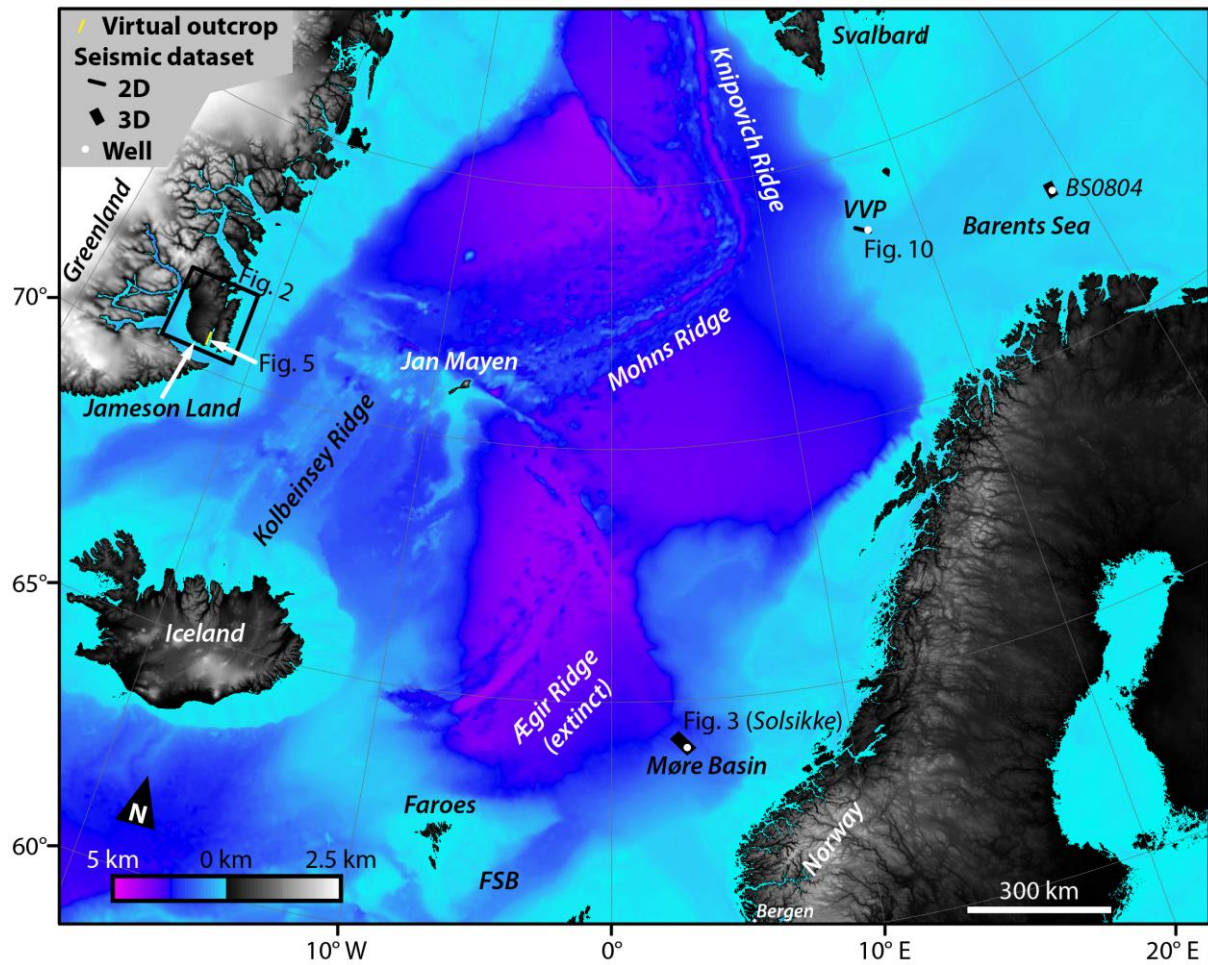
Fig. 1: Map of the conjugate margins around the Norwegian-Greenland Sea, showing locations of datasets used for this study. FSB, Faroe-Shetland Basin, VVP, Vestbakken Volcanic Province. Topography from the ETOPO grid (Amante and Eakins, 2009).
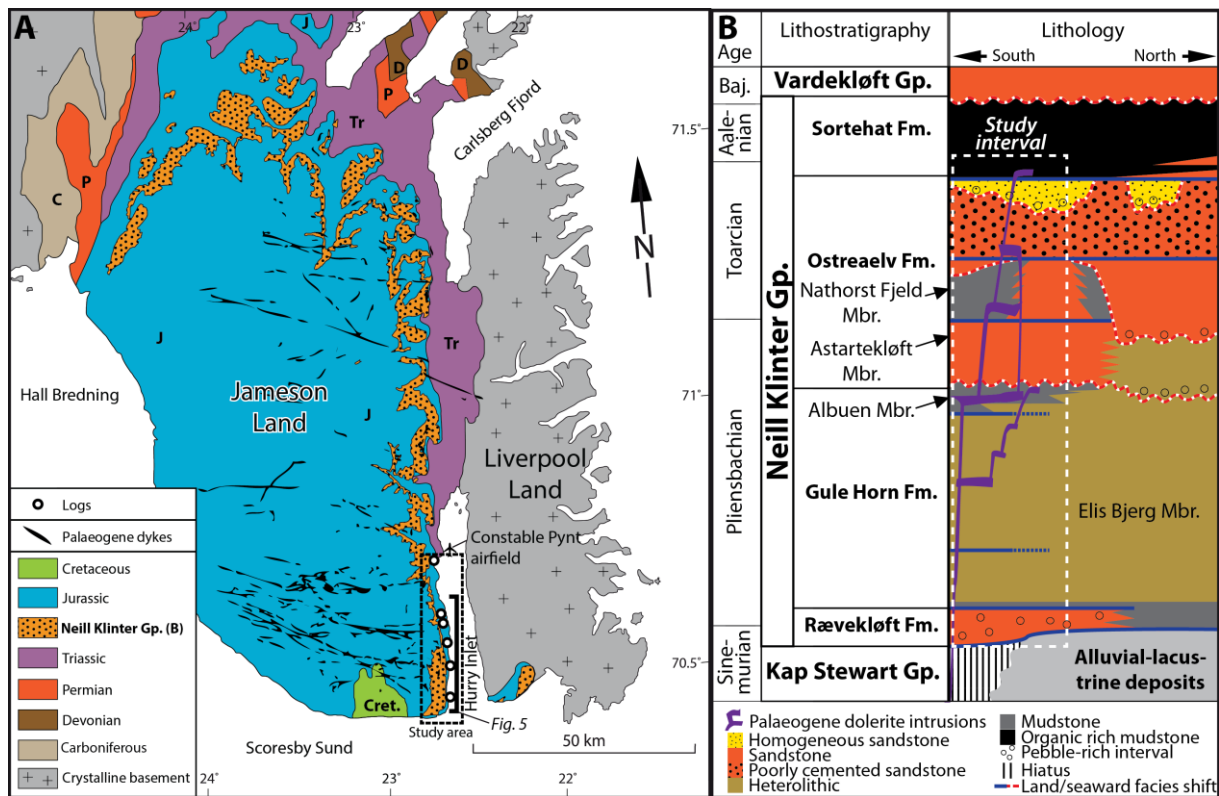
Fig. 2: Location and setting of the main outcrop dataset. See Fig. 1 for location. A) Geological map of the study area, modified from Ahokas et al., 2014. Note occurrence and orientation of dykes. B) Lithostratigraphy of the studied Jurassic Neill Klinter Gp. modified from Ahokas et al. (2014) and Eide et al. (2016).

Studies of large-scale architectures of igneous intrusions are commonly based on seismic data. Studies of the architecture of igneous intrusions in outcrops that have a scale comparable to reflection-seismic data (100s of m high, tens of km long) are rare (e.g. Muirhead et al. 2012, 2014; Eide et al., 2017; Walker et al. 2017), and the link between the large-scale architecture investigated in seismic studies, and the detailed observations possible in outcrop studies has not yet been explored in detail. In particular, it is difficult to know how features of sill-complexes imaged in seismic reflection data relate to actual geometries of sill-complexes within the subsurface (e.g. Magee et al., 2015). This is important, as observation of fine-scale sill features may increase subsurface predictivity (e.g. Schofield et al 2012a; Eide et al 2017). Seismic imaging issues occur due to three inherent limitations in the

3D seismic method (Figs. 3, 4): (1) decrease of seismic quality and resolution with depth due to absorption of high frequencies, seismic energy and downward increase in seismic velocity (Fig. 3A, 4D, e.g. O'Brien and Lucas, 1971; Planke et al., 2005); (2) overburden effects, where the seismic signal is affected by complex overburden which can be a considerable problem in basins with igneous rocks (Fig 3C, e.g. Fliedner and White, 2003; Hanssen et al, 2003; Ziolkowski et al., 2003; Gallagher and Dromgoole, 2007; Fernandes, 2011; Flecha et al., 2011; Holford et al., 2012; Schofield et al., 2015; Planke et al., 2015); and (3) the inability of the reflection seismic method to image steeply dipping and vertical interfaces (c.f. Fig. 4D and 4E; e.g. Lecomte et al., 2016).
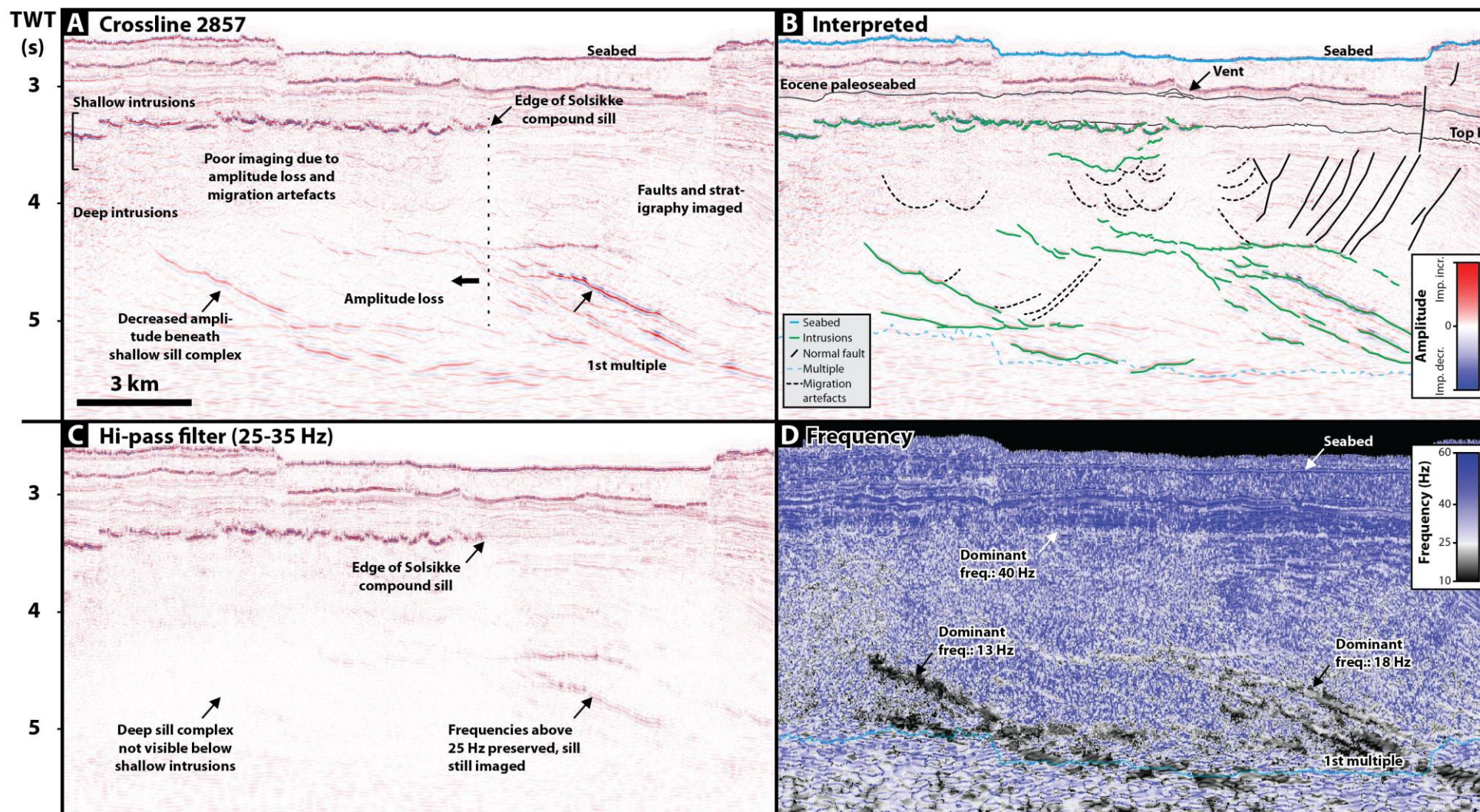
Fig. 3: 3D seismic line illustrating common problems in imaging of deeply emplaced sill-complexes. For location, see Fig. 1. A) Uninterpreted seismic line. Note the shallow intrusions, which mainly appear as compound saucer-shapes, and the deeper intrusions, which show more layer-parallel and branching geometries. Also note the poor imaging below the shallow intrusions, and the general decrease of resolution and definition with depth. B) Interpreted version of (A). K, Cretaceous. C) High-pass filtered version of (A) with a filter sloping from 35 to 25 Hz. Note loss of high frequencies below the shallow intrusions. D) Frequency plot of (A). Note the high dominant frequencies in the upper part of the survey, lower frequencies in the lower part, and the decrease in frequency below sills compared to in areas without overlying sills.

Furthermore, available reflection seismic data from areas with sill-complexes are commonly not processed in ways that are optimal to preserve important details in such systems. Processing of seismic data is inherently computer intensive, and therefore a compromise is often sought between the time it takes to produce an acceptable result for a particular prospective interval, against the time it take to process the data. More processor-intensive migration algorithms which can image complex subsurface structure more accurately, such as reverse time migration (Gray et al. 2001), are therefore often not employed (e.g. Hardy et al., 2008; Fernandes, 2011).
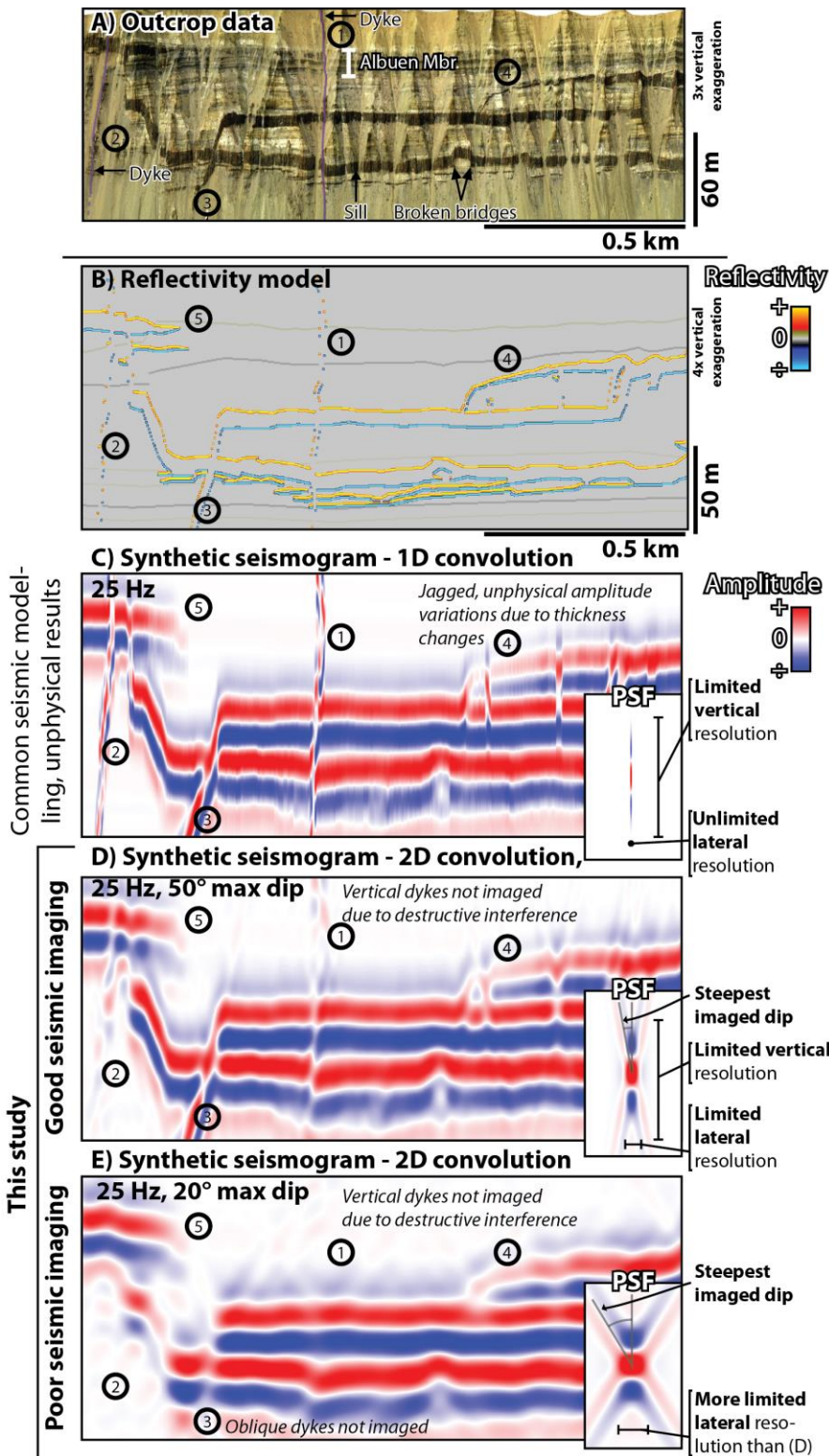
Fig. 4: Figure illustrating the seismic convolution method, the difference between 1D and 2D convolution, and the concept of point-spread functions (PSF). A) Outcrop data from Jameson land. Intrusive rocks appear as dark bands in the cliffs. This section is located from 6-9 km in Fig. 5. B) Reflectivity model, generated from outcrop architectures and acoustic properties from relevant wells (Table 1A). C) Synthetic seismogram generated using the reflectivity model in (A) convolved with the 1D 25 Hz Ricker wavelet shown in the inset. Using this method, the lateral resolution is vastly

overestimated and equal to the trace spacing. Dipping interfaces are shown to be imaged even though they would not be in actual seismic. D) Synthetic seismogram generated using 2D convolution and high (50°) maximum imaged dip-values. This simulates good-quality seismic with the ability to image relatively steeply dipping interfaces. E) Synthetic seismogram generated using 2D convolution and low (20°) maximum imaged dip-values. This simulates poor-quality seismic which does not have the ability to image steeply dipping interfaces. In particular, note these main issues: (1) Near-vertical dykes are well-imaged in synthetic seismic based on 1D convolution, but are not imaged well due to destructive interference in the 2D-convolution cases. (2, 3) Steeply dipping (c. 45°, 30°) dykes are not imaged in poor-quality seismic. (4) Because adjacent traces do not influence each other in 1D convolution, the reflectors show a jagged and unphysical amplitude variation, which are not be present in the 2D convolution models. (5) Abrupt terminations of reflectors are not imaged perfectly as in (C), but are actually diffuse as in (D) and (E).

In this paper, we investigate how an outcropping example of a Paleogene sill-complex intruded at c. 3 km depth in Jurassic sedimentary rock (Figs. 1, 2; Eide et al., 2016; 2017) would be imaged in seismic data in various simulated scenarios. Synthetic seismic data was generated from actual sill geometries, using methods that explicitly model both limited vertical and lateral resolution and take the inability to image steeply dipping structures into account (Lecomte et al., 2016). We also compare our results to actual seismic from the conjugate Norwegian Margin (Fig. 1), which has experienced significant volcanism related to onset of sea-floor spreading and later readjustment of plate motion (Talwani & Eldholm, 1977; Saunders et al 1997; Faleide et al 2008). The goals of this study are threefold: (1) To investigate how sill-complexes emplaced in sedimentary rocks are imaged in seismic data; (2) to investigate how overburden complexity affect imaging of sill-complexes; and (3) to discuss what these results imply for the interpretation of sill-complexes in seismic data and prompt a discussion amongst the seismic imaging community similar to what took placed for improvement of imaging beneath extrusive volcanics sequences in the late 90's and early 00's (c.f. Ziolkowski et al 2003; Gallagher and Dromgoole, 2007; Flecha et al., 2011).

1.1 Synthetic seismograms of sill-complexes - issues and previous work

In order to investigate how actual sill geometries would be imaged in seismic data, synthetic seismograms can be generated from field data or conceptual models. Synthetic seismic data are routinely generated by constructing a reflectivity model, extracting one-dimensional (1D) vertical traces along this model, convolving these traces with a wavelet to obtain seismic traces (referred to as 1D convolution), and visualizing these traces as synthetic seismograms (Fig. 4c; e.g. Widess, 1973; Smallwood and Marsesh, 2002; Thomson, 2005; Magee et al., 2015). However, although such methods give a good, first-order impression of seismic imaging in areas of little lateral variation, such methods are unsuited to investigate seismic imaging of complex geology because they vastly overestimate lateral seismic resolution, (e.g. Lecomte et al., 2016), such as in the case of salt diapirs, fold-and-thrust belts, or in this case, igneous sill-complexes. The 1D convolution method leads to three particularly noteworthy artefacts (Fig. 4) that would not be present in actual 'real-world' reflection seismic data. Firstly, reflector terminations of geological units (e.g. sills) will be much more pronounced than they will be in actual seismic data (Point 5 in Fig. 4). Secondly, steeply dipping interfaces will be imaged perfectly (i.e. dykes), in contrast to actual seismic which is not adept at imaging steeply dipping interfaces (Points 1, 2 and 3 in Fig. 4). Thirdly, tuned reflector packages (i.e. sills that are so thin that the reflections from top and bottom interfere and create a compound reflection, c.f. Widess, 1973) will exhibit pronounced amplitude variations which relate to thickness-variations, as amplitudes in seismograms made using 1D convolution methods will be extremely sensitive to short-wavelength thickness changes (e.g Point 4 in Fig 4). All the listed effects above will be much more diffuse in real seismic data, because the lateral resolution is limited and the response from a single sampled point will be influenced by adjacent points. Therefore, utilising 1D convolution alone could lead to

significant misunderstandings if lessons learned from analysis of such synthetic seismic data are used to guide interpretation of real seismic data.

Intrusions which are emplaced into unconsolidated sediments (commonly at depths <1.5-2 km) often show saucer-shaped morphologies (Fig. 3; Hansen and Cartwright, 2006a; Galland et al., 2009; Schofield et al 2012a). Such intrusions are generally well-imaged and well understood, as these often occur shallowly and without overlying high-velocity layers. However, architectures of sills emplaced within cemented and lithified sedimentary rocks (commonly at depths > 1.5-2 km) have been subject of much fewer studies than their shallow counterparts, and their architectures thus are less understood (Schofield et al., 2012a; Eide et al., 2017). Furthermore, sills emplaced deeper (<1.5-2 km) in sedimentary basins are often more poorly imaged in seismic data due to a thicker overburden and overlying intrusions (Fig. 3). Overlying igneous material (i.e. high velocity layers) leads to reflection and absorption of seismic energy (e.g. Planke et al 2015), and greater depth leads to attenuation of the seismic signal particularly at high frequency ranges (Fig. 3c, d; e.g. O'Brien and Lucas, 1971; Hanssen et al., 2003; Gallagher and Dromgoole, 2007). Additionally, refraction, diversion and spreading of large-incidence ray paths occur below high-velocity layers, which leads to both lower resolution and inability to image steeply dipping features at depth (e.g. Purnell, 1992; Smallwood and Maresh, 2002).

In sum, the issues presented above commonly lead to intrusions which are not imaged at all, intrusions that are imaged as tuned reflector packages (making thickness estimates difficult), multiple intrusions imaged as a single one due to interference effects, and unimaged steeply dipping features. Such effects become more pronounced with increasing depth. This is a problem, as it gives considerable uncertainty in the interpretation of

subsurface sills and sill complexes, with regards to sill volume, sill architecture, sill thickness and sill-induced host-rock maturation.

2. Geological setting

The synthetic seismic data generated in this study is based on architectures of igneous intrusions and host-rock from a field area near the SE margin of the Jameson Land Basin (Fig. 2) in East Greenland (Eide et al., 2017). The host-rock sandstones, mudstones and sparse conglomerates were deposited in the Early-Middle Jurassic during a post-rift thermal sag phase (Surlyk, 2003), and comprises a variety of siliciclastic shallow-marine tide-influenced sedimentary rocks, deposited close to the basin margin (Dam and Surlyk, 1998; Ahokas et al., 2014; Eide et al., 2016). The Jameson Land Basin was a minor sub-basin in the Mesozoic seaway between Norway and Greenland, and the sedimentary host-rocks are time- and facies equivalent to the Båt Group, which is a prolific reservoir interval on the conjugate Haltenbanken area on the Norwegian Continental Shelf (Martinius et al., 2001; Ichaso and Dalrymple, 2014; van Capelle et al., 2017). Late Jurassic-Cretaceous rifting and Paleogene volcanism led to deposition of c. 3 km of sediment and lava flows above the study interval (Brooks, 1973, 2011; Larsen and Marcussen, 1992; Mathiesen et al., 2000; Surlyk, 2003). Deposition of a significant overburden led to quartz-cementation and lithification prior to emplacement of igneous intrusions (Hald and Tegner, 2000). The studied sill-complex is an example of intrusions emplaced into brittle sedimentary rock, rather than into unconsolidated sediments. This distinction is important, as shallow intrusions emplaced in sediments commonly show ductile emplacement features and develop saucer-shaped acthiceatures, while intrusions in sedimentary rocks show brittle emplacement features and show more planar architectures (Schofield et al., 2012a; Eide et al., 2017).

The studied sills are part of the mafic Jameson Land Suite, and consist of nonvesicular, aphyric tholeiitic dolerites with ophitic texture (Hald and Tegner, 2000), and vary in thickness from c. 1 – 18 m, with an average thickness of 9 m (Eide et al., 2017). The architecture and morphology of the sills is clearly influenced by the host-rock lithology, as they favoured intrusion along mudstone intervals, avoided well-cemented homogeneous sandstone units, and show clear ductile/non-brittle emplacement features such as peperite and elliptical fingers within sparse poorly-cemented sandstone intervals (Eide et al., 2017). For the purpose of this study, the intrusives and Jurassic host-rock can be divided into seven facies associations (Figs. 2B, 5; Table 1): 1: Paleogene *dolerite intrusives*, 2: *Homogeneous sandstone*, 3: Bedded *sandstone* with thin mudstone intervals, comprising > 50 cm thick sandstone beds and 0.1-5 cm mudstone beds, 4: *Poorly cemented sandstone*, due to the presence of chlorite overgrowths (c.f. Ahokas et al., 2014), 5: *Heterolithic* beds, comprising interbedded 1-50 cm thick sand- and mudstone beds with a variable but overall approximately equal proportion of sandstone and mudstone, 6: regionally extensive *mudstone* intervals, and 7: *organic rich mudstone* intervals (c.f. Krabbe et al.,1994).

The sills in Jameson Land are an example of a small-volume (c. 10% of studied outcrop sections) sill-complex intruded at a depth of 3 kminto what was mainly brittle, layered host-rock, which has subsequently been uplifted (Mathiesen et al., 2000; Eide et al., 2017). This is in contrast to many exposed examples of sill-complexes around the world. For example, sills in the Karoo Basin of South Africa are associated with somewhat larger intrusion volumes, and were emplaced at shallower levels, where the host-rock was not well consolidated (Schofield et al., 2010; Svensen et al., 2015). Other relatively well-studied examples, such as the sills emplaced in the Theron and Transantarctic Mountains of Antarctica were emplaced at a similar depth and in similar lithologies, but are the results of much higher intrusion volumes as these attain thicknesses of up to 330 m (Hersum et al., 2007; Jerram et al., 2010).

The architecture and depth of intrusion of the Jameson Lands Suite makes it broadly comparable to intrusions seen at deep levels (~ 3-4 km), in the present day contemporaneous basin fill along the NE Atlantic Margin around the Base Cretaceous/Top Jurassic (c.f. Schofield et al., 2015).
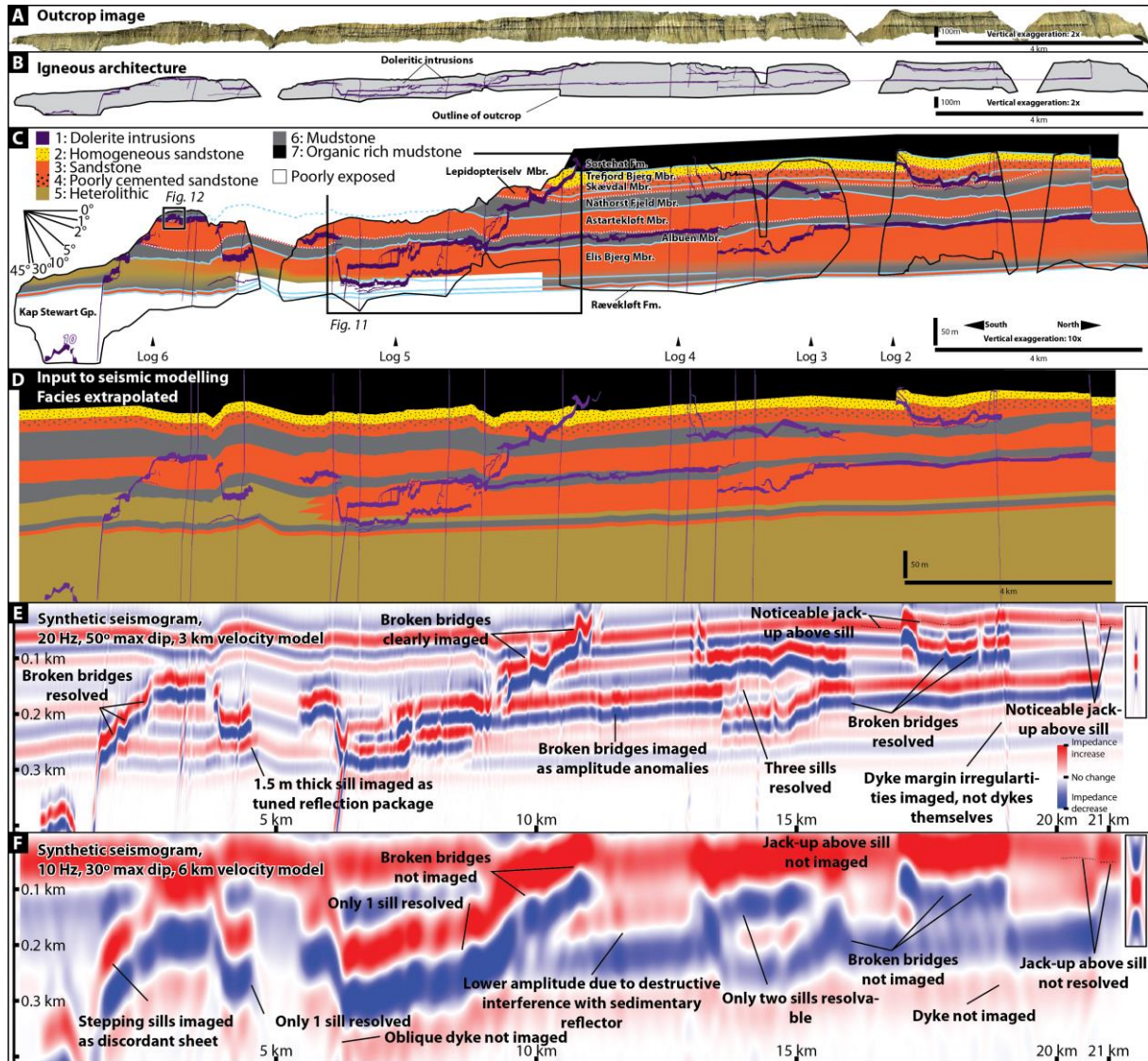

Fig. 5: Outcrop data and synthetic seismograms. For location, see Figs 1, 2. A) Studied outcrop. B) Igneous architecture from outcrop. C) Stratigraphic and igneous architecture. Note the tendency for intrusions to follow mudstone units, the consistent upwards-stepping of intrusions in other lithologies than mudstone, and the jack-up of host-rock above sills. D) Input model to seismic modelling, populated with acoustic properties from Table 1. E) Synthetic seismogram corresponding to model A in Fig. 7. F) Synthetic seismogram corresponding to model C in Fig. 7.

Table 1: Input data for modeling. NCS, Norwegian Continental Shelf; MD, measured depth, FA; Facies association.

a) Values for target at 1 and 3 km depth

Name	Facies association #	V_P km/s	V_P/V_S fraction	Density g/cm3	Source NCS well/article	Depth MD (m)
Igneous intrusions	1	6.3	1.86	3.0	Smallwood and Maresh, 2002	
Homogeneous sandstone	2	3.7	1.80	2.5	Add 5% to FA3	-
Sandstone	3	3.5	1.80	2.4	6407/2-1	3220-3235
Poorly cemented sandstone	4	3.4	1.80	2.3	Subtract 5% from FA3	-
Heterolithic	5	3.3	1.80	2.3	6407/2-1	3030-3050
Mudstone	6	3.8	1.80	2.5	6407/2-1	2920-2940
Organic rich mudstone	7	2.6	1.80	2.3	6407/2-1	2885-2900

b) Values for target at 6 km depth

Name	Facies association #	V_P km/s	V_P/V_S fraction	Density g/cm3	Source NCS well/article	Depth MD (m)
Igneous intrusions	1	6.3	1.86	3.0	Smallwood and Maresh, 2002	
Homogeneous sandstone	2	4.8	1.80	2.7	Add 5% to FA3	-
Sandstone	3	4.6	1.80	2.6	6506/12-10A	5525-5545m
Poorly cemented sandstone	4	4.4	1.80	2.4	Subtract 5% from FA3	-
Heterolithic	5	4.7	1.80	2.5	6506/12-10A	5565-5582m
Mudstone	6	4.7	1.80	2.4	6506/12-10A	5618-5635m
Organic rich mudstone	7	3.9	1.80	2.5	6506/12-10A	5330-5335m

3. Sill architecture in studied outcrop section

The sedimentary and igneous architecture of the studied outcrop in Jameson Land is shown in Fig. 5. A variety of features noteworthy for the present study occur in this section, and these are summarized from Eide et al. (2017): Individual sills are broadly layer-parallel and constitute c. 10% of the material in the outcrop section. *Main sills* make up 70% of the intruded volume, and these are 7-12 m thick, with average thickness of 9 m. Where *main sills* propagate in other lithologies than mudstones, less than 2 m thick *sill splays* occur within 10 m from the margins of the main sills (Eide et al., 2017).

The type of host-rock (*mudstone*, *brittle interbedded sandstone and mudstone*, *brittle homogeneous sandstone*, and *poorly cemented sandstone*) is a major controlling factor on the architecture of sills. The host-rock has been classified into 7 *Facies Associations* (FA, c.f. Table 1; Eide et al., 2017). The majority of sills (c. 60%) are emplaced within regionally extensive mudstones units (FA6). Within these regional mudstones, sills mainly follow a single stratigraphic layer where they show very sparse *step-* and *broken bridge-*features and attain lengths of up to 6 km. Sills emplaced in well-cemented interbedded sandstone (FA 2) and mudstone (FA 5) make up c. 25% of sill volume, and show abundant intrusive *steps* and *broken bridge-*structures (c.f. Figs. 4A; 6; see also Eide et al., 2017) and cross-cut stratigraphy and propagate towards regional mudstones (Fig. 5C). Broken bridge structures form as two vertically offset and laterally overlapping sills inflate, bend the host-rock "bridge" formed between them, which ultimately break and creates a through-going, magma-filled conduit (Hutton, 2009; Fig. 6). Broken bridges are important indicators for magma propagation directions (Schofield et al., 2012a), and unbroken bridges may form pathways for hydrocarbon migration. Sills in other lithologies constitute a minority (15%) of the intrusive material in the outcrop, but show complex splaying geometries in homogeneous sandstones

(FA2), and both ductile (peperite and elliptical fingers) and brittle emplacement features in poorly cemented sandstones (FA4).
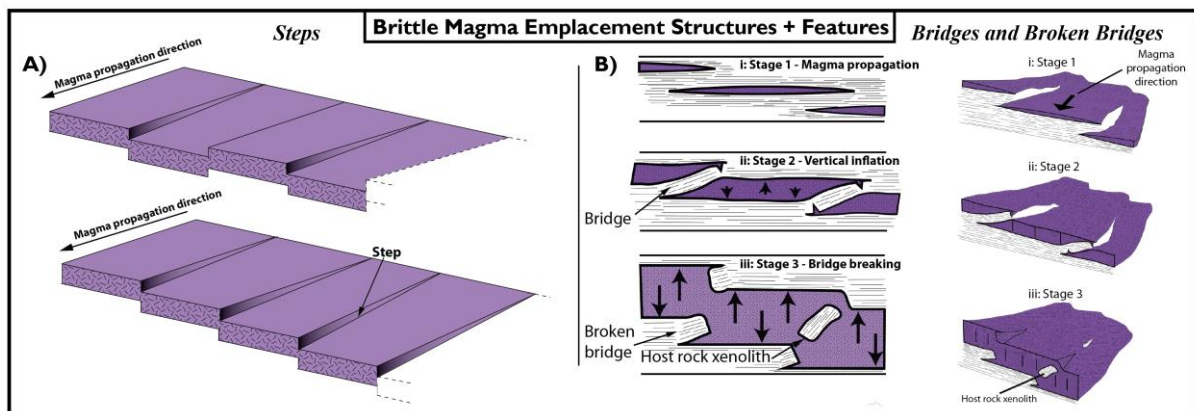

Fig. 6: Overview of sill structures and features formed during emplacement and progressive inflation of sill intrusions in brittle host-rock. A) Expression of steps on sill margins and how they relate to the magma propagation direction. B) Development of broken bridges through vertical inflation of sills and breaking of host-rock bridges between sill segments. Modified from Schofield et al. (2012a).

E-W-trending, near-vertical (dip > 80°) dykes occur in the study area (Figs. 2A; 5C), and these vary from 1-10 m wide, and only a small number of these are interpreted to postdate the main intrusive phase based on cross cutting relationships, the rest of the dykes are believed to be coeval with the sills as radiometric ages are coherent and cross-cutting relationships are not observed in these (Hald and Tegner, 2000). Together, sills and dykes compartmentalize the host-rock into intrusive-bounded blocks c. 0.2-4 km wide and 20-120 m thick.

Intrusion of c. 10% of igneous material into the outcrop volume appears to be solely accommodated by 1:1 uplift of host-rock above sills, as no deformation of the rock apart from sill intrusion is observed. This is shown as stratigraphy restores without error by removing the sills from images taken orthogonal to the plunge of the beds (Eide et al., 2017, their fig. 10). This indicates that deeply emplaced sills (>1.5-2 km) formed as fractures which inflated vertically in a piston-like fashion (c.f. Gilbert 1877; Hunt et al, 1953; Johnson and

Pollard, 1973). This does not apply to intrusions within the the poorly-cemented Skævdal Mbr (Fig. 5b), which makes up 9% of the studied outcrop, where intrusion of material was also partly accommodated by ductile deformation of the host-rock.

The sum of these observations show that sill-complexes have complicated architectures and that details of the architecture might have significant implications for sill emplacement, reservoirs and hydrocarbon systems (c.f. Rateau et al. 2013; Senger et al., 2017). How these details are imaged in seismic data will be studied in the remainder of this contribution.

4. Methods and dataset

4.1 Outcrop data

The synthetic seismic models are based on analysis of the Jameson Land Suite mafic sill-complex and surrounding host-rock of the Neill Klinter Group, imaged in a 22 km long and 250 m high virtual outcrop model (Figs. 2A, 5A) acquired using oblique helicopter-mounted LIDAR-scanning. The outcrop model was acquired using the Helimap System (Vallet and Skaloud, 2004), using a laser scanner, a digital medium format camera with a 35 mm lens, and an inertial navigation system. Processing of these data (see Buckley et al., 2008; Rittersbacher et al., 2014; Eide et al., 2016) yielded a high-quality virtual outcrop model with 0.3 m point spacing and a pixel resolution of c. 7 cm. The outcrop model is constrained by a set of six sedimentary logs with a total thickness of 1040 m. The outcrop is oriented north-south, and is a strike-section through the sedimentary systems (Dam and Surlyk, 1998). Apart from a general proximal-to-distal trend leading to more fine grained deposits southwards in the outcrop throughout all stratigraphic units, the lateral lithological variability is low (Fig. 5C; Dam and Surlyk, 1998; Eide et al., 2016), leading to a good constraint on lithology, and ultimately petrophysical properties used for modelling, in the entire dataset. The outcrops

are generally unfaulted, tectonic dip is on average 3° towards the west, and the sills are generally parallel to sedimentary layering.

Interpretations of sedimentary units and intrusions on the virtual outcrops from Jameson Land yielded scaled, georeferenced lines which have been projected onto a plane parallel to the outcrop and orthogonal to the plunge of the tectonic dip of layers. As the lateral lithological variability is quite low (Eide et al., 2016), extrapolation of stratigraphy and sill architecture into unexposed areas was straightforward (Fig. 5D).

4.2 Synthetic seismic modelling

The synthetic seismic models of the studied section yield data that simulate zero-phase, pre-stack depth-migrated (PSDM) reflection seismic data (Lecomte et al., 2015). The methodology applied for modelling is based on ray-tracing modelling for study of the overburden effects (Gjøystdal et al., 2007; Fig. 7), and on 2D convolution (Fig. 4) for the generation of synthetic seismic models of the target interval (c.f. Lecomte et al., 2016). Detailed reviews of these methods are out of scope of this paper and therefore only briefly summarised here.

Four main parameters are critical for the seismic modelling presented in this study: rock P-wave velocity, rock density, seismic frequency at the target depth, and maximum imageable dip of strata (*max dip*) at the target depth. In reality, these parameters vary with the depth of the modelling target, the geological history of the target and overburden, and the overburden architecture. P-wave-velocity and density of host-rock and overburden are taken from relevant depths in time-equivalent formations on the Norwegian Continental Shelf (Table 1), and P-wave-velocity and density for igneous intrusions is from Smallwood and Maresh (2002). Seismic frequency at the target depth is measured from a publically available

3D seismic dataset from the Møre Basin (NH003, "*Solsikke*") in the base case, and from the BG0804-survey in the Barents Sea in the case of an eroded basin (Fig. 8). It is worth pointing out that vertical resolution in seismic data is a function of the signal frequency and host-rock velocity, while the lateral resolution is a function of signal frequency, host-rock velocity and illumination, here expressed as max dip of imageable strata (e.g. Lecomte et al. 2015, c.f. Figs 4D, E). For each of the different overburden scenarios (Fig. 6), the post-migration lateral resolution has been modelled. The maximum imaged dip of strata (max dip) for each of the models has been investigated using ray-tracing methods (Fig. 6), and the seismic frequency has been investigated in comparable datasets (Fig. 7).
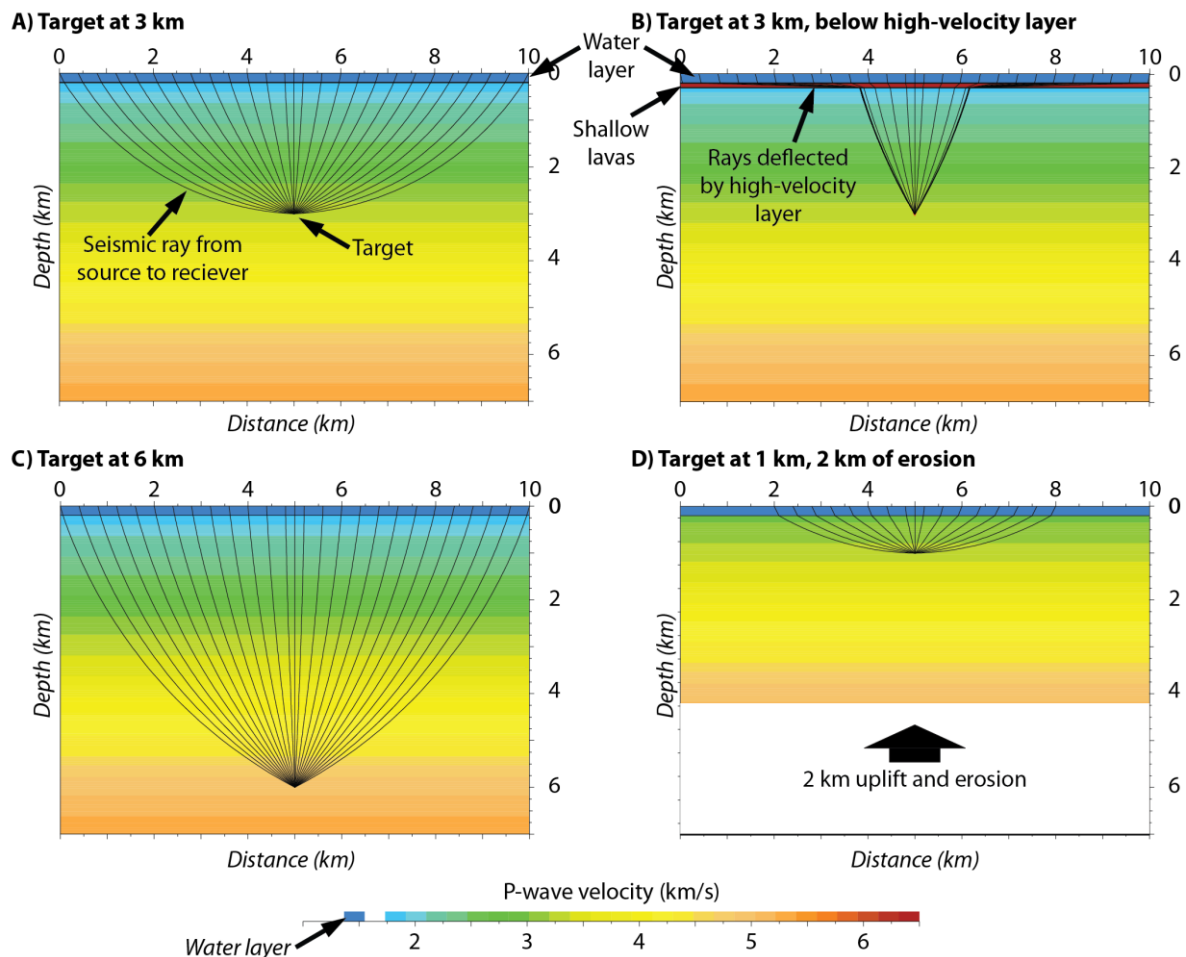

Fig. 7: Overburden models, generated to investigate ray propagation and resulting lateral resolution for each of the cases. Interfaces hit by rays with a large variety of incidence angles will have high lateral resolution, and more steeply dipping interfaces are imaged. A) Model with linear P-wave velocity gradient based on well data from the Norwegian Continental Shelf. B) Model with a linear P-wave velocity gradient and an overlying high-velocity layer (i.e. shallow intrusions, lavas). Note the steep incidence of rays reaching the target, resulting in low lateral resolution. C) Model with linear P-wave

The seismic modelling procedure utilized in this paper consists of the following steps: (1) Four different conceptual overburden models are created using specified layer interfaces, velocity gradients and petrophysical properties derived from relevant wells from the Norwegian Continental Shelf (Fig. 7). (2) Wave-propagation from seismic source, through the overburden model, to the target depth, and then back to receivers is simulated based on ray-based algorithms in order to investigate maximum imageable dip of strata, which is used to define a two-dimensional spatial "wavelet" (termed Point-Spread Function (PSF), c.f. Fig. 4) based on dominant frequency of the signal at depth of interest. (3) Creation of a target reflectivity model using layer architectures obtained from outcrop analysis (Fig. 5D) and petrophysical properties from appropriate subsurface analogues in wells (Table 1). (4) 2D convolution of the target reflectivity model with the PSF obtained in Step 2.

4.3 Overburden models

This section contains an overview of imaging parameters (max dip and dominant frequency) based on the four overburden scenarios presented in Fig. 7). All models are constructed with a 0.2 km thick water layer, and a linear P-wave-velocity gradient from 1.8 km/s at the seabed, 3.3 km/s at 3 km, and 4.8 km/s at 6 km.

Model A (simple overburden) investigates a base-case, where the target intrusions are simply overlain by 3 km of sedimentary host-rock (Fig. 7A).

Model B (overlying igneous rocks) investigates the influence of an overlying high-velocity layer, here modelled as a 100 m layer of basalt at the seabed (Fig. 7B). Other geometries of overlying high-velocity layers (a 100 m thick sill at 200 m; both a 100 m thick sill at 200 m and a 100 m layer of basalt at the seabed) have also been modelled, and gave similar results.

Model C (deep burial) tests the effects of further burial of the target interval to 6 km (Fig. 7C), resulting in increased host-rock velocity at the target interval (Table 1B).

Model D (uplifted and eroded basin) tests the effect of 2 km of erosion of the overburden (Fig. 7D), yielding a P-wave velocity of 2.9 km/s at the seabed and a target at 1 km depth where the average seismic velocity is 3.3 km/s.

4.3.1 Seismic frequency

Frequency attenuation with depth is difficult to model well, and signal frequency versus depth is therefore taken from the *Solsikke* 3D seismic survey from the Møre Basin (Fig. 1) for models without erosion (Fig. 7A-C). Shallow sills, presently at c. 1 km below the seabed, are imaged at c. 40 Hz. Deeper intrusions at c. 3 km below the seabed, are imaged at c. 18 Hz, which is similar to what is observed in other localities on the N Atlantic Margin, such as in the Faroe-Shetland Basin (Schofield et al. 2015), where the sills occur at relatively deep levels within the contemporaneous basin fill. Significant attenuation of high frequencies (>25 Hz) occur just below shallow sills (c.f. Fig. 3). At depths of c. 3 km in areas underlying shallow sills, the dominant frequency is c. 13Hz, a significant reduction compared to 18 Hz in areas without overlying sill intrusions (Fig. 8B). For model D, where 2 km of overburden has been eroded, frequency versus depth has been taken from the BG0804-survey in the Barents Sea (Fig. 1) where the depth of erosion is similar (Henriksen et al., 2011; Baig et al., 2016), and a number of exploration wells provide excellent depth control. At c. 1 km depth, the dominant frequency is 40 Hz (Fig. 8B).
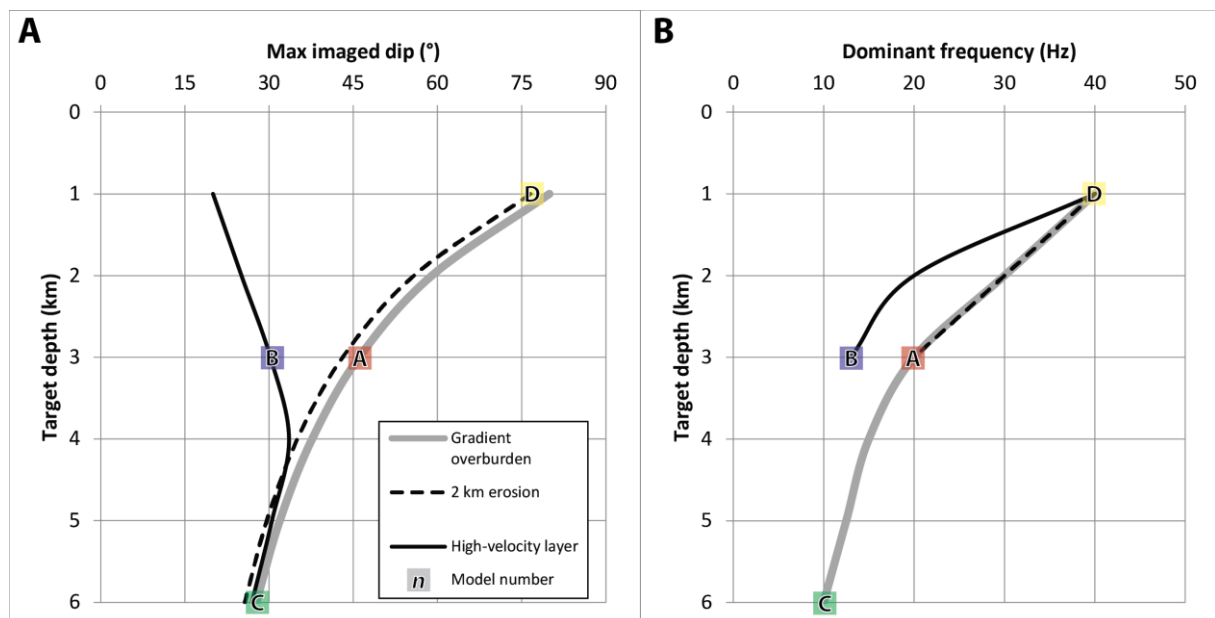

Fig. 8: Imaging properties used for generation of synthetic seismograms in Figs. 5, 9 and 10. Inset letters show properties at target depth corresponding to cases in Fig 7. A) Max imaged dip calculated from models in Fig. 7. B) Dominant frequency at depth, derived from analysis of 3D seismic datasets.

4.3.2 Illumination and overburden effects

The main goal of the overburden modelling is to investigate the maximum imageable dip of strata and thus also the lateral resolution which can be expected to occur in different cases and at different depths. Using a ray-tracing approach, lateral resolution in seismic data is a function of the max dip, and this is illustrated in Fig. 4. The modelling shows that the models can be grouped into three groups which behave similarly (Fig. 7):

Models with a simple overburden (Fig. 7A,C) have high max dip (and hence good lateral resolution) at shallow depths (c. 80° at 1 km), and decrease rapidly to c. 45° at 3 km and 30° at 6 km.

In the models with high-velocitiy layers above the target, only rays with steep incidence angles may reach the target, as lower-incidence angle rays are refracted away from the target (Fig. 7b). This leads to a significant reduction in max dip, to c. 30° at 3 km depth (Fig. 8A).

In the models with 2 km erosion, the maximum imageable dip is close to, but slightly higher than models with a simple velocity-gradient in the overburden (Fig. 7A). The strong velocity contrast at the seabed caused by a hard sea-floor will increase the potential for strong multiples. This would lead to potentially worse imaging than is accounted for here, and more complex and costly processing of actual seismic surveys acquired in such settings.

4.3.3 Summary of overburden effects

In summary, the modelling of overburden effects and inspection of publically available 3D-seismic data from relevant basins indicate that for models with a simple gradient overburden, seismic frequency and max dip decrease gradually with depth (Fig. 7). For models with overlying high-velocity layers such as lavas and/or shallow intrusions, a sharp decrease in max dip and high-frequency content occurs once the seismic waves hit the high-velocity layers. This leads to poorer imaging of underlying features, such as sill-complexes. The eroded models show a moderate worsening in lateral resolution, and a frequency-loss with depth comparable to models with simple gradient.

5. Remarks on seismic resolution and detectability of sills

5.1. Seismic Resolution and Amplitude of Igneous Intrusions

In order to understand issues with imaging igneous sills and sill-complexes in reflection seismic data, seismic resolution and seismic detectability must be discussed. The limited range of frequencies available in seismic surveys leads to limitations in the lower limit of bed thicknesses that may be uniquely resolved (e.g. Widess, 1973; Kallweit and Wood, 1982; Simm and Bacon, 2014). The limit of thickness of beds that may be resolved is termed vertical resolution, and the seismic resolution is commonly approximated to be ¼ of the dominant wavelength ($\lambda = v_P / f$) of the signal, however, the exact value is dependent on the wavelet shape (e.g. Simm and Bacon, 2014). This is illustrated in Fig. 9, where imaging of a 100 m thinning dolerite and mudstone wedge is simulated using a 2D point-spread function (PSF). Using a PSF based on a Ricker wavelet, onset of tuning occurs at $\lambda/3$ (c. 45 m). At thicknesses greater than 45 m both the top and the bottom of the wedge is imaged as separate reflectors. Thus, the bed is not *resolved* at thicknesses smaller than c. $\lambda/3$ (45 m).

As the bed thickness approaches $\lambda/4$ (35 m), the side-lobes of the lower reflection start to interfere constructively with the main lobe of the upper reflection. This leads to a greater amplitude in this thickness range. At wedge thicknesses smaller than c. $\lambda/3$, the thickness of the wedge may not be determined from the reflected signal, and this is known as the *tuning effect* or the *tuning thickness* (e.g. Kallweit and Wood, 1982). The distance between the amplitude peaks of the upper and lower reflections (Fig. 9B) does not change as the wedge thins past the tuning thickness in Fig. 9D. In this thickness range, the main lobe of the upper reflection interferes constructively with the side-lobes of the underlying reflection, the reflection amplitude increases to a peak of c. 1.4x the normal amplitude. The highest amplitude due to constructive interference (peak tuning) occurs at c. $\lambda/5$ (28 m).

As the dolerite wedge thins further than the peak tuning thickness of $\lambda/5$, there is an overall decrease in the amplitude strength, first because the side-lobe and main lobes interfere in a non-optimal way, and then as the oppositely-directed upper and lower main lobes starts to interfere with each other. In the modelling run presented in Fig. 9, there is a gradual decrease of amplitude strength as the wedge thins further. It is important to note that the reflection amplitude at $\lambda/11$ (11 m) is equal to the reflection amplitude at the top of a dolerite reflector which is not tuned.
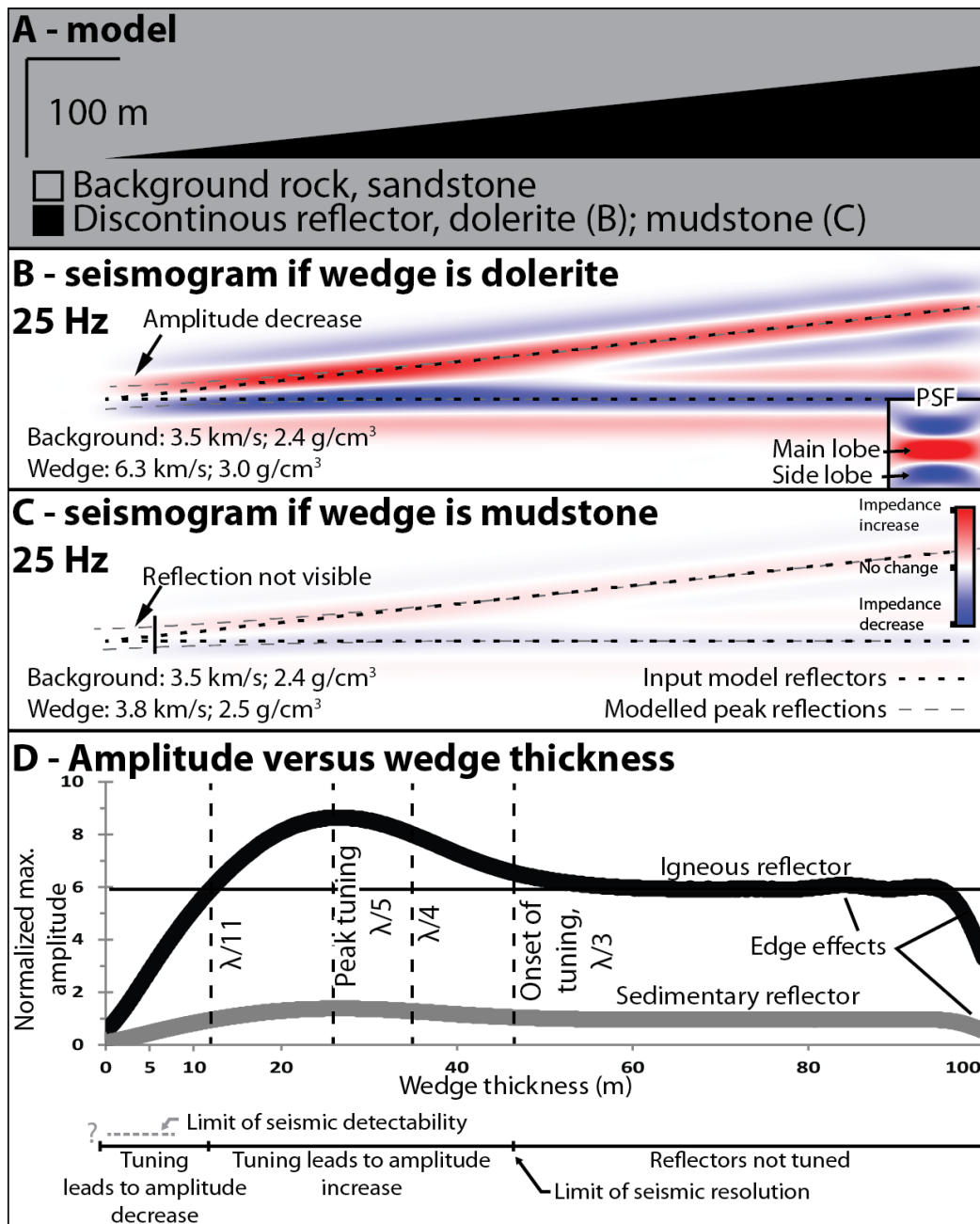
A - model

100 m

☐ Background rock, sandstone
■ Discontinous reflector, dolerite (B); mudstone (C)

B - seismogram if wedge is dolerite

25 Hz   Amplitude decrease

Background: 3.5 km/s; 2.4 g/cm³
Wedge: 6.3 km/s; 3.0 g/cm³

PSF
Main lobe→
Side lobe→

C - seismogram if wedge is mudstone

25 Hz   Reflection not visible

Impedance increase
No change
Impedance decrease

Background: 3.5 km/s; 2.4 g/cm³
Wedge: 3.8 km/s; 2.5 g/cm³

Input model reflectors - - - -
Modelled peak reflections – – –

D - Amplitude versus wedge thickness

Normalized max. amplitude

λ/11   Peak tuning λ/5   λ/4   Onset of tuning, λ/3

Igneous reflector
Edge effects
Sedimentary reflector

Wedge thickness (m)

Limit of seismic detectability

?

Tuning leads to amplitude decrease   Tuning leads to amplitude increase   Reflectors not tuned
Limit of seismic resolution

Fig. 9: Wedge-model illustrating the concepts of seismic tuning, seismic resolution and seismic detectability. Wavelength (λ) = 140, λ/4 = 37.5 m. A) Input model geometry. The model is 1 km long, and contains a 900 m long wedge thinning towards the left from 100 to 0 m. B) Resulting seismogram at 25 Hz using the inset PSF for a wedge consisting of dolerite within sandstone. Note the clearly resolved top and basal reflectors for wedge thicknesses from 100-45 m, the increased amplitude and overestimated thickness due to seismic tuning from 45-12 m wedge thickness, and the rapid amplitude decrease for wedge thicknesses of 12-0 m. C) B) Resulting seismogram at same conditions and amplitude scale for a mudstone wedge within a sandstone. Note the decreased amplitude compared to (B), and the lack of visible reflections at wedge thicknesses smaller than c. 10 m. D) Graphs showing normalized maximum amplitude per trace for (B) and (C). Note the similarity in the seismic signal for intrusions which are c 40 m thick and c. 10 m thick, indicating that relatively thin intrusions such as the ones in this study would be nearly indistinguishable from thicker intrusions in seismic data as long as the intrusions are thinner than seismic resolution.

5.2 Seismic detectability of sill intrusions

The *seismic detectability* of an interface relates to whether a reflection from an interface can be recognized in seismic data or not. Rules-of thumb have been suggested for detection limits of sills based on sill thickness. For example, Planke et al. (2005), stated that although the detection limit is difficult to quantify, it can be approximated to $\lambda/10$. However, seismic detectability is a much more difficult issue to address than seismic resolution, as it is a function of many more variables than just the sill thickness, some of which are poorly constrained and difficult to model. In order to detect a reflection, it must have a significantly higher amplitude than the baseline set by seismic noise in a survey. As seismic data is subject to significant amounts of processing to remove noise, it is hard to provide definitive answers without knowing each particular case, but we can offer some general considerations.

The amplitude of a reflection depends on the contrast in acoustic impedance (P-wave velocity × density) across the layer interface. It follows from the input values used in this study (Table 1), that dolerite intrusions have much higher P-wave velocity and density than their sedimentary host-rocks. Thus, the amplitudes from the top of igneous intrusions are much higher than amplitudes from sedimentary reflectors. This is shown in Fig 9, where the amplitude of a reflector from a sandstone-dolerite interface is about 6 times higher than the amplitude of a sedimentary reflector, all other things being equal. It is important to note that the focus of this paper is intrusions of a mafic composition (i.e. dolerites) emplaced within siliciclastic rocks, which are most commonly encountered in the North Atlantic (e.g. Smallwood and Maresh, 2002). More felsic intrusions such as andesites and granites have lower density and P-wave velocity (Rybach and Buntebarth, 1984), leading to lower impedance contrast with surrounding host rocks, which in turn leads to lower seismic amplitudes which makes them more difficult to detect. Such intrusions are also more viscous than dolerites, potentially leading to other architectures.

Assuming that the data quality of a seismic survey is good enough to image a siliciclastic sedimentary reflector at depth, it follows from the wedge model in Fig. 9D that it should be theoretically possible to image and detect reflections even from very thin dolerites (i.e. thicknesses down to a few meters). Furthermore, it also follows that sills with a thickness in the order of $\lambda/11$ (11m) would be imaged with the same reflection amplitude as an un-tuned reflection from a sediment-dolerite interface (Fig 9D). This implies that igneous intrusions with thicknesses similar to those in the studied cliffs in East Greenland (on average 9 m)

should be easy to detect in seismic. This is supported by Sheriff and Geldart (1995) who suggested that low-amplitude hydrocarbon-bearing sandstone within mudstones could be detected seismic data of "reasonable data quality" at thicknesses of λ/20 – λ/30. Because these *rules-of-thumb* are determined with reflections from siliciclastic reflections in mind, and because of the much greater acoustic impedance contrast between dolerite and siliciclastic rocks, we suggest that a limit of detectability of λ/30 is probably too pessimistic *in principle* for what can be detected in good-quality seismic data. However, in reality, combined seismic and well-log datasets from areas with igneous intrusions commonly reveal large amounts of un-imaged sill intrusions (c.f. Fig. 10, Schofield et al., 2017). In the following sections, we investigate this.
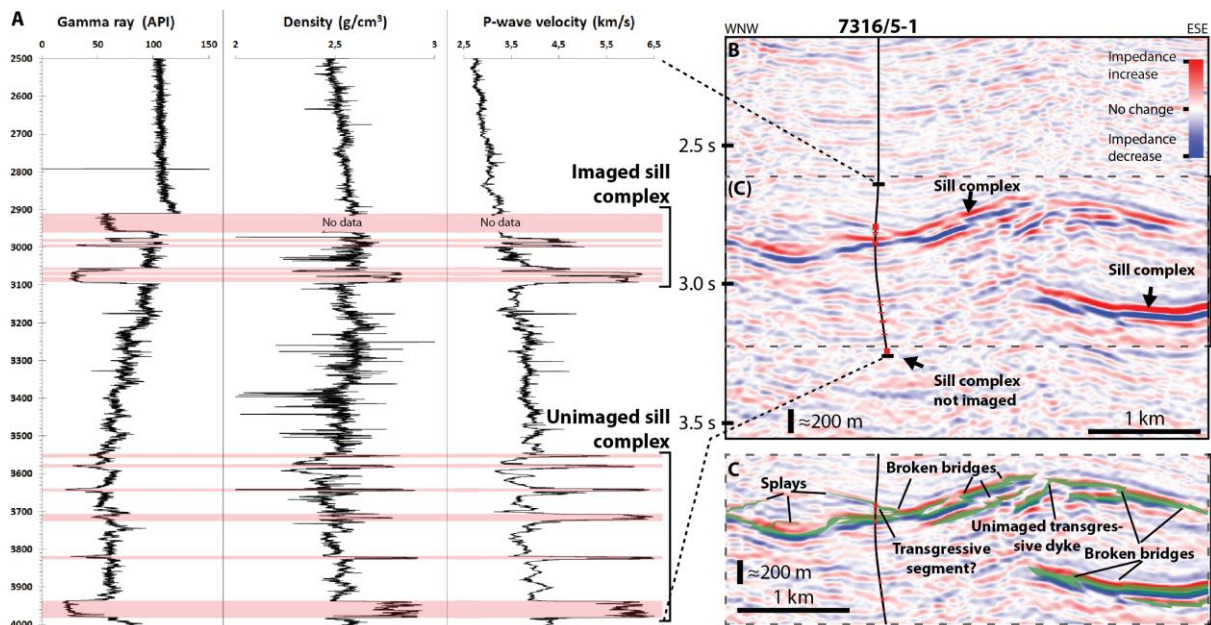

Fig 10: Comparison of well and seismic data of sill-complexes. A) Data from well 7316/5-1 from the Vestbakken Volcanic Province on the W Barents Sea Margin. Red fields show depths of interpreted igneous intrusions. B) Uninterpreted seismic section around the well in (A). Note that only the upper sill-complex is imaged, although the lower sill-complex is of similar thickness. Red fields on well indicate intrusions in (A). C) Interpreted section from B. Note the similarity of the actual seismic data to the synthetic seismograms generated from outcrop data from E Greenland, and that geometries of seismic reflectors corresponds to geometries observed in outcrop.

6. Forward seismic modelling

6.1 Base case: imaging at 3 km depth, simple overburden

In this base case, we investigate how the studied sill and sedimentary architecture (Fig. 5D would be imaged using the chosen properties (Table 1) at 3 km depth with a simple overburden (Fig. 7A). For an overburden model with a linear velocity gradient, a target at 3 km depth, and an average host-rock P-wave velocity of 3.1 km/s at the target, the modelling indicates that high-quality, depth-migrated, zero-offset seismic data will appear similar to Fig. 5E. Despite the modest thickness of main sills (7-16 m) and relatively low seismic frequency (20 Hz) the sills are still clearly imaged in the synthetic seismogram (Fig. 5E), with reflections from the intrusions showing much higher amplitudes than reflections from sedimentary interfaces. Tuning thickness (e.g. Kallweit and Wood, 1982; Brown, 2011) is commonly taken as a quarter wavelength, which in this case (V_P=3.1 km/s, f=20 Hz) is c. 40 m. Even sills as thin as 1.5 m are detected as amplitude anomalies (Fig. 5E at 4.5 and 13 km), but it is possible that these would not be detected in actual seismic data due to presence of noise.

The architecture of the sill-complex is generally well-constrained in the synthetic seismogram (Fig, 5E), and both sills and oblique dykes with dips shallower than 45° are imaged. Broken bridges (c.f. Fig. 6) with large offsets (15 m) are clearly imaged as large steps in the simulated reflections, while broken bridges with offsets smaller than 15 are imaged as local amplitude anomalies in otherwise continuous reflections (Fig. 11C, 12C). It is possible that these amplitude anomalies caused by small-offset (< 15 m) broken bridges could not be separated from seismic noise in real seismic data. The steps observed on the investigated sill margins are not detectable in the seismograms (Fig. 11C; 12A), and this is probably due to the small step heights in this dataset, which are 2 m on average. In this seismogram (Fig. 11C), the broken bridges would be indistinguishable from larger-offset steps. Each sill in this seismogram is generally imaged separately (Fig. 11C), as they are spaced more widely (c. 30 m) than ½ seismic wavelength (c. 20 m). Thin sills, on the scale of less than a few meters, are imaged as complex interference patterns (9.2 km in Fig. 11C).
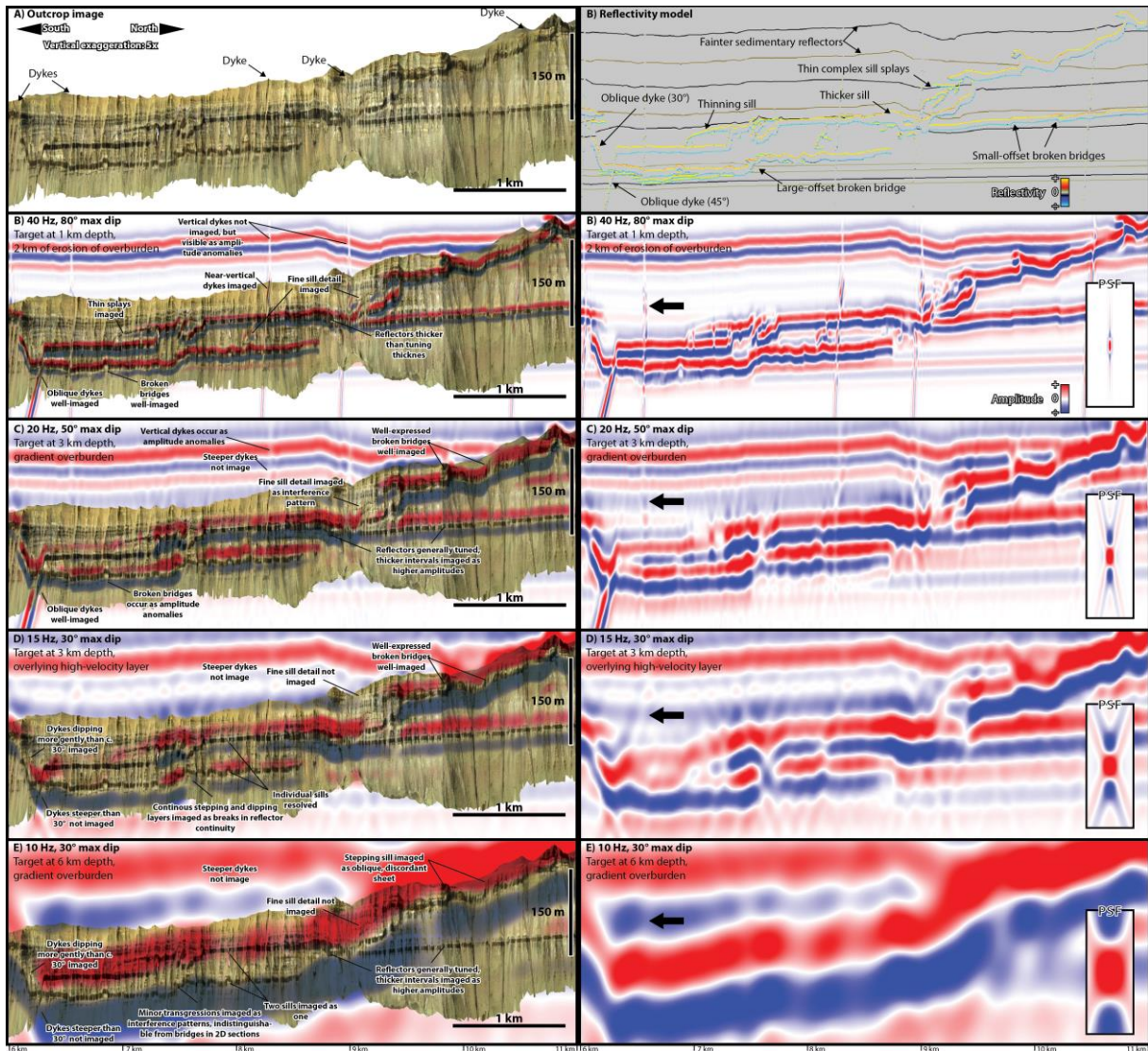
Fig. 11: Comparison of details of synthetic seismograms. Distances along the outcrop are the same as in Fig 5. See Fig. 5C for location, and Appendix A2 and A3 for high-resolution versions. A) Outcrop image and reflectivity model. B) Synthetic seismogram corresponding to model D in Fig. 7. C) Synthetic seismogram corresponding to model A in Fig. 7. D) Synthetic seismogram corresponding to model D in Fig. 7. E) Synthetic seismogram corresponding to model C in Fig. 7. Note that this model is generated using velocity model B in Table 1.

Steeply dipping to vertical igneous features (> 50°) i.e. dykes, are not imaged directly in this seismogram, but dykes are still detected in the seismogram (Fig. 11C). This is mainly due to two reasons: (1) dyke margin irregularities are imaged instead of the dykes themselves, and (2) dykes lead to disruptions in original layer continuity that leads to discontinuities in the seismic data that may be interpreted as dykes. In simulations with lower lateral resolution, dykes are not detected (Figs 11D,E).

Pronounced jack-up of host-rock above sills is common in the dataset from Jameson Land Greenland (Eide et al., 2017). This is detected in the synthetic seismogram, particularly near the top at 17 and 21 km (Fig. 5E), where the reflections from the sedimentary bedding are clearly offset across dykes and transgressive sills.

6.2 Deep imaging: target at 6 km depth, simple overburden

For a target at 6 km depth, increased seismic velocity and density due to increasing compaction and diagenesis must be taken into account (Table 1B). For an overburden model with a linear velocity gradient, a target at 6 km depth, and an average host-rock P-wave velocity of 4.5 km/s, the modelling indicates that high-quality, depth-migrated, zero-offset seismic data will appear like in Fig. 5F. In this case, the dominant frequency would be c. 10Hz, yielding a tuning thickness of c. 100 m. Individual main sills (7-16 m thick) to the left of the seismogram are imaged, but where several sills occur together towards the right (right of 7 km in Fig. 5E) the reflectors coalesce and the entire sill-complex appears as one single, complex reflector. This composite reflector shows the highest amplitudes of all reflections in this seismogram due to the large amplitude contrast between intrusives and host-rock. However, at depths of 6 km, the amplitude contrast between host-rock and intrusives are smaller compared to the models at 3 km depth. This is because increased burial will lead to increased compaction and cementation of the host rock (e.g. Sclater and Christie, 1980), causing reduced acoustic impedance contrasts through reduction in velocity and density contrast between the dolerite intrusions and host rock (c.f. Table 1). In addition significant local amplitude decreases due to destructive interference occur, particularly between dolerite intrusions and the overlying reflection generated at the interface between the Astartekløft Member and Nathorst Fjeld Member (e.g. at 12 km in Fig. 5F).

Prominent stepping sills, such as at 2 and 9 km along the profile (Fig. 5F), are imaged as oblique sheets which are discordant to bedding. Broken bridges are in some instances imaged as amplitude anomalies, but these are generally indistinguishable from amplitude anomalies generated by interference with reflections from host-rock stratigraphy. Due to loss of lateral resolution at depth, oblique dykes dipping more than c. 30° are not imaged (Figs. 5F at 7 km; 9E).

In several cases, such as at 7 km along Fig. 5F, closely spaced sills only generate one compound reflection, and individual sills are therefore not resolvable. Jack-up of host-rock above sills at the scale observed in this outcrop (c. 8 m) is not detected (Fig. 5F). Through inspection of the seismograms generated in this study, it appears that jack-up of stratigraphy on the scale of 1/30 of a wavelength could be detected in data of comparable quality.

6.3 Imaging below high-velocity layers

The seismogram in Fig. 11D was generated to simulate imaging of the profile in Fig. 5D at 3 km depth, below shallow igneous intrusions within an otherwise simple overburden (Fig 6B). Reduction in both the seismic frequency ($\lambda/4 = 25$ m) and lateral resolution (max dip = 30°) below shallow sills is evident when comparing the broadening and thickening of the point-spread-functions in the insets in Figs 11C and 11D. In the corresponding seismograms, it is striking to note the decrease in lateral resolution, and therefore the loss of ability to image more steeply dipping interfaces (c.f. Figs. 11D and 11C). Broken bridges are not well imaged anymore, and stepping sills rather occur as oblique sheets. Steeply dipping oblique dykes (>35°) are not imaged, and amplitude anomalies related to presence of vertical dykes are no longer observed because of the low lateral resolution. Furthermore, decreased frequency leads to less well-defined reflectors. Imaging of fine-scale features such as steps and broken bridges with varying frequency and lateral resolution is covered in Fig. 12.

6.4 Shallow imaging

The seismogram in Fig. 11B was generated in order to simulate imaging of the profile in Fig. 5D at 1 km depth, which would be the result of emplacement of the intrusives at 3 km depth, followed by 2 km of post-magmatic erosion (Fig 6D). Provided that seismic acquisition-problems related to hard seafloor can be overcome, modelling resulted in a seismogram with high frequency and high lateral resolution (Figs. 11B). In particular, compare the point-spread-function of this seismogram to the others (insets in Fig. 11). In this case, the synthetic seismogram shows a remarkable similarity to the input model, due to the high

frequency and the high max dip, yielding good lateral and vertical resolution. Tuning thickness (19 m) is close to the sill thickness, and a clear relationship between thinning of sills and decrease in amplitude occurs. Steeply dipping interfaces, broken bridges and steps are clearly imaged, and even some meter-scale sill-splays are detected.
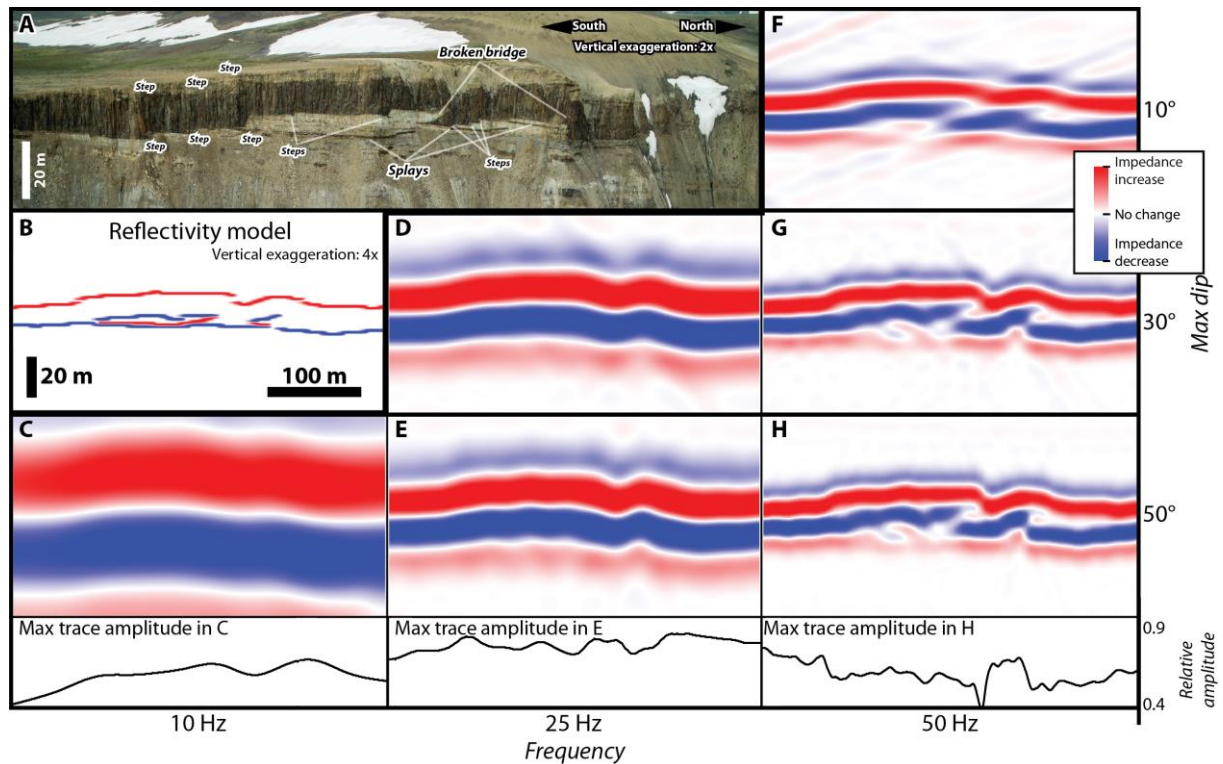

Fig. 12: Seismic imaging of broken bridges, steps and sill splays. See Fig. 5C for location. A) Outcrop image showing abundant splays, steps and broken bridges. B) reflectivity model generated from (A). C-H) Synthetic seismograms showing imaging with different lateral resolution (expressed as max imageable dip) and dominant frequency. Note especially the influence of a decrease in lateral resolution (F, G and H).

7. Discussion

7.1 Modelling limitations and seismic noise - When can we not see intrusions at all?

In all types of modelling, there are limitations and simplifications. The method applied here has significant advantages compared to methods used for modelling igneous intrusions in previous studies (e.g. Magee et al 2015), particularly because this model takes limitations in horizontal resolution into account, because it includes the effect of overburden on seismic imaging at the target, and because it more accurately represents steeply dipping features such as dykes. The method applied in this study also has two particular limitations (which would also be present in 1D convolution) that should be pointed out before inferences made from analysis of the synthetic seismograms are applied to actual seismic data, (1) a difficulty in correctly represent steep features in grid-based models, and (2) lack of noise.

7.1.1 Dykes and near-vertical interfaces

Near-vertical (> 70°) interfaces such as steeply dipping dykes are modelled as a series of vertically offset points rather than continuous reflectors (Fig 4B). This is because reflection coefficients are calculated vertically in a grid. Furthermore, the theoretical background of ray-based seismic imaging and processing assumes relatively flat layers. However, the dykes modelled in this study (e.g. Fig 5E) appear as linear lows in amplitude, resembling interpreted dykes in seismic data elsewhere (Wall et al., 2010; Minakov et al., 2017, their fig. 5), showing that the representation of dykes in the model achieves realistic results.

Interestingly, in seismic data with low lateral resolution (e.g. Fig. 11D, E), stepping sills are imaged as oblique sheets. Also, because the impedance contrast between intrusives and host-rocks is so high, very little interference-effects between the layered host-rock and the

oblique intrusions are observed. This is in contrast to modelling results reported by Magee et al (2015), who used 1D convolution and lower velocities for igneous intrusions (5.55 km/s). In these models, interference between seismic signals from inclined igneous sheets crosscutting planar sedimentary layers led to lead to apparent steps ('*pseudosteps*') in the modelled seismic images. These apparent steps from models were compared to steps in actual seismic data of intrusions cross-cutting planar sedimentary layers, and these steps were hypothesised to be an artefact rather than actual steps (c.f. Magee et al 2015, their fig. 14). In our models, we see the opposite effect: Initially stepped intrusions are imaged as inclined sheets because the lateral resolution of seismic is too low to image the steps (2 and 8 km in Fig. 5F). This difference likely occurs because the model employed by Magee et al (2015) employed 1D convolution, which dramatically overestimates horizontal resolution (c.f. Fig. 4), and a much lower velocity contrast. In well-data from the North Atlantic, sills generally have velocities at c. 6.2-6.3 km/s (Fig. 10, Smallwood and Maresh, 2002), and amplitude contrasts between sills and sediments are higher. We therefore expect 'pseudosteps' to be of little importance in the North Atlantic, especially in seismic data below c. 1.5 km where horizontal resolution is lower and sill velocities are higher. The risk of encountering pseudosteps might be greater in shallow seismic where lateral resolution is greater and in settings with lower impedance contrast between sills and intrusions (i.e. more andesitic sills).

7.1.2 Noise

The simulated seismograms are generated without simulating acquisition noise. However, the simulated seismic images are not simply smoothed versions of the input models, but do contain several examples of discontinuous reflectors, dipping noise and amplitude variations which are not part of the input models, but that rather the results of simulation of diffractions occurring at discontinuities of reflectors. Fig. 11 contains abundant examples of

this, and particularly noteworthy examples occur in the lower right part of Figs. 11C and D, where diffractions from broken bridges in the lower sill interfere with underlying planar sedimentary reflectors.

In all models, the modelled reflections from the sill intrusions are coherent and show considerably stronger amplitudes than sedimentary reflectors. In all cases, even in Model D (Fig. 11E) which simulates imaging at 6 km depth, the reflections from the intrusives are detectable. In this case, the background seismic velocity is c. 4.5 km/s, the signal frequency is 10 Hz, and consequently, the wavelength of the signal is 465 m. This means that onset of tuning occurs at sill thicknesses of c. 150 m. The sills in the study area are c. 10 m thick ($\lambda/47$), and will in this case give stronger reflections than an un-tuned sedimentary reflector. However, if acquisition noise was also modelled, would the intrusives be detectable? This is a difficult question to answer, because it is difficult to model acquisition noise in a rigorous manner (Scales and Snieder, 1998). Random noise could of course be added, but the detectability of the reflections would depend on the amplitude of the noise, which would be entirely arbitrary because no good way of estimating the amplitude of noise in processed seismic data exists. Still, the modelling shows that as long as reflections from sedimentary interfaces are imaged, reflections from even relatively thin sills (more than a few meters) should be imaged as well.

7.2 Comparison to real data

A number of important issues are highlighted as the results from this study are compared to actual reflection seismic data.

7.2.1 Thickness and tuning

The vast majority of published examples of sill intrusions imaged in seismic data occur as tuned reflectors (e.g. Smallwood and Maresh, 2002; Thomson, 2005; Cukur et al., 2010; Schofield et al., 2012b; Haafez et al., 2017; Schmiedel et al., 2017). Only a few examples of

sills where also the basal reflection is imaged separately are published (e.g. Hansen and Cartwright, 2006b; Jackson et al., 2013; Schofield et al., 2015). In deep and low-frequency seismic data, there is also the possibility that what is imaged as one reflector is in fact a reflection of several stacked sills (e.g. Schofield et al., 2015; Magee et al 2017), as in the example of Fig. 5F. This illustrates that seismic reflection data have the potential to significantly overestimate the thickness of discrete sills in a basin.

7.2.2 Un-imaged sills, and applications to seismic interpretation

The modelling and discussion above indicates that, theoretically, even thin sills at thickness of $\lambda/50$ should be imaged in seismic reflection data, even at relatively deep (> 3 km) basinal levels. However, many real world datasets combining well- and seismic data shows that large amounts of sills are in fact not imaged at all (e.g. Fig. 10). For example, Schofield et al (2015) demonstrated that only a small number of the sills identified in well data from the Faroe-Shetland Basin are actually imaged in seismic data.

A similar relationship can be seen in seismic data from the Vestbakken Volcanic Province at the western Barents Sea Margin (Figs. 1, 10). Exploration well 7317/5-1 encountered 12 sills of doleritic composition which are clearly identifiable in wireline well logs (Fig. 10A, Omosanya et al., 2016). These igneous intrusions make up an upper and a lower sill-complex. While the upper complex (with sill thicknesses measured in the well ranging from 5 to 47 m) is relatively well imaged in seismic data, the lower sill-complex, consisting of intrusions ranging in thickness from 5 to 43 m, is not imaged at all in the well location (Fig. 10B).

In an ideal scenario within the subsurface, a single, continuous body of dolerite, with sharp contacts with surrounding host rock may be well imaged potentially down to very small thicknesses. However, in reality sill-complexes do not consist of single continuous bodies, but often rather of several complex, interconnected sills and thinner sill splays (Figs. 5C, 13; e.g. Thomson and Hutton, 2004; Galerne et al 2011; Muirhead et al., 2014; Magee et al., 2014; 2016; Schofield et al., 2015; Walker et al., 2017; Eide et al., 2017). In the case of sill-complexes with large amounts of thin intrusions (c.f. Fig. 13E, Schofield et al., 2015, their fig. 6B), reflections from the thin intrusions may interfere with each other and yield no coherent reflections (Fig. 13E).

Significantly, sill complexes can also possess large lateral variations in effective velocity, as a result of splitting of individual intrusions and separate discrete intrusions being present within the subsurface (Fig. 13). The resulting lateral velocity profile can therefore be highly variable, even over relatively short distances (10's of m, c.f. Figs. 5C, 13E). Some seismic imaging techniques, like Kirchhoff Time Migration, are not well-suited for areas with large lateral velocity changes (Gray et al 2001; Fernandes, 2011). As a consequence, migration artefacts can occur, which may fully mask underlying, weaker reflections from sills or stratigraphy.
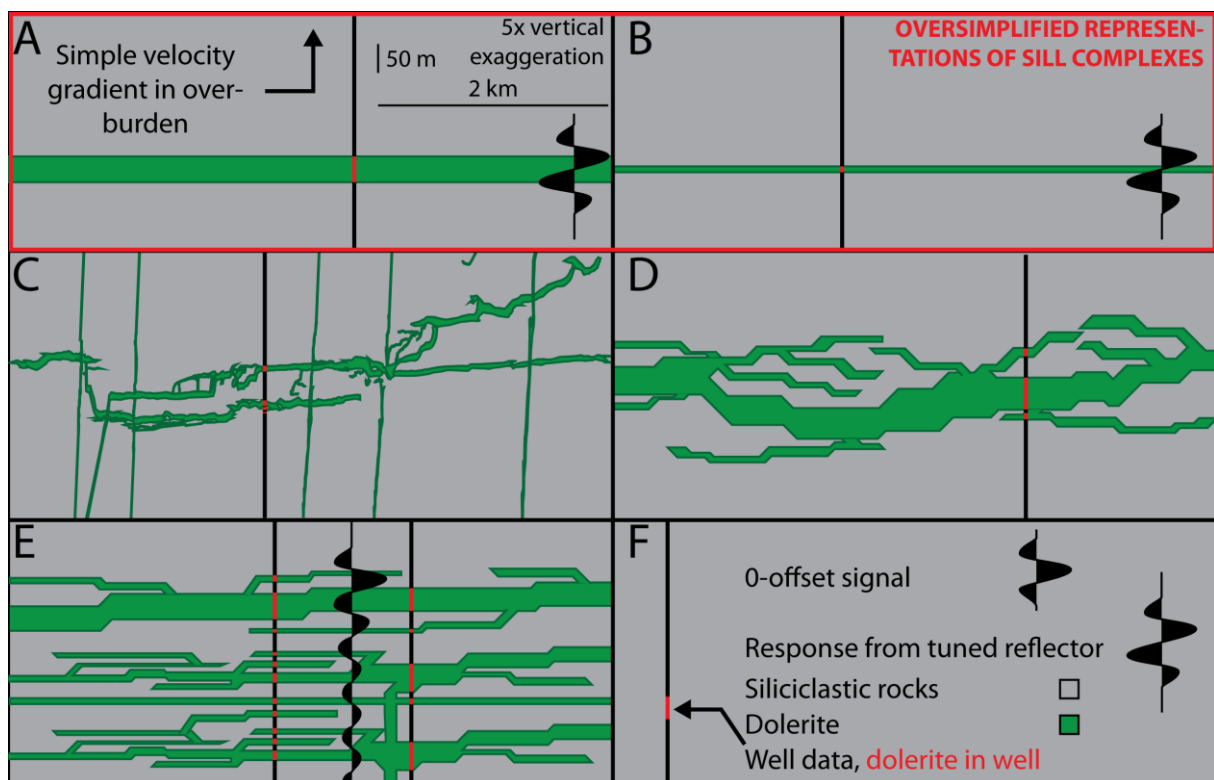

Fig 13: Comparison of conceptual geometries of sill-complexes, where individual sills are below seismic tuning thickness. A) Simple and unrealistic tabular sill, just below tuning thickness. B) Simple and unrealistic tabular sill, with a thickness of ¼ of the tuning thickness. Note that these are imaged at comparable amplitudes. C) Real-world example of a small-volume sill-complex, from Fig. 11A. D) Conceptual diagram of a larger-volume sill-complex. Note large lateral variability in thickness and amount of dolerite. E) Conceptual diagram of a High-volume sill-complex consisting of abundant thinner sills and splays. This example would likely give a strong reflection at the top, and weak and incoherent reflections below the top due to interference below seismic resolution. F) Legend.

7.3 Future Perspectives: "The Sub-Sill Imaging Problem"

Considerable work has been done on the so-called 'sub-basalt imaging problem', which has yielded substantial results over the last 15-20 years, but has been mainly focussed on imaging beneath extrusive lava sequences (c.f. Ziolkowski et al 2003; Gallagher and Dromgoole, 2007; Flecha et al., 2011). However, significantly more sedimentary basins contain extensive igneous sills, than large basaltic piles (e.g. South Australian Margin; Holford et al. 2012). Despite this, there is little awareness of the specific issues and challenges relating to imaging of sill intrusions, and in particular imaging below sill-complexes, termed the 'Sub-Sill Imaging Problem' (Fernandes, 2011). As accurate basin modelling relies on a good appreciation of source rock extent and thickness within a sedimentary basin, and given that in many sedimentary basins, potential source rock intervals (and occasional reservoirs) are inferred to occur below sill-complexes, it may be time for the community to specifically address the imaging issues faced around the 'Sub-Sill Imaging Problem' (e.g. Hanssen et al 2003; Fernandes, 2011; Planke et al 2015).

Within this paper we have attempted to show the complexities of sills and the effect this has on seismic imaging. Importantly, synthetic seismic modelling presented in this paper indicates that relatively thin igneous sills could potentially be imaged in reflection seismic data. However, inspection of available datasets shows considerable migration artefacts below shallow intrusions, which points towards poor representation (and possible understanding?) of sills and geometries in velocity models used in seismic processing.

Imaging of igneous dykes is also probably hampered by a lack of awareness of the importance of these. Such discontinuous features, when viewed in a processing phase, may be simply regarded as seismic artefacts and subsequently removed. This is a problem, as these can act as significant barriers or conduits to hydrocarbons and other basinal fluids, depending on post-emplacement evolution (e.g. Rateau et al. 2013; Senger et al., 2015; Eide et al., 2017). Seismic modelling performed in this contribution indicates that these could potentially be imaged in seismic data, and tentative interpretations of dykes have been made in regional seismic lines (Wall et al., 2010; Minakov et al., 2017).

Computational intensive migration algorithms, like Reverse Time Migration, are potentially better at imaging intra- or sub-sill strata (e.g. Gray et al., 2001; Hardy et al. 2008; Fernandes,

2011). However, any migration model is only as good as the velocity model used, which in turn is only as good as the understanding of the sub-surface geology. Therefore, improvement of imaging requires a greater predictive understanding of where sills will appear in sedimentary basins, better methods to predict architecture of sill-complexes, in addition to understanding the effect heating by the intruding magma had on the velocity of surrounding host rock.

Until now, conceptual understanding of sill-complexes drawn from analysis of field data has essentially only been applied for the interpretation of seismic data. Such insights could also lay the foundations for progress in seismic processing and imaging and addressing of the 'sub-sill imaging problem'. Geologists who interpret seismic data commonly receive seismic datasets without knowing much about the data acquisition, data processing, and importantly, what constraints these steps put on imaging and understanding of the dataset. It is important that geologists request information about constraints from data processing and acquisition, maximum dip of imageable strata at different depths, and interval velocity models. It is equally important that this information is provided by geophysicists.

8. Conclusions

This study has investigated how mafic sill-complexes emplaced within sedimentary basins are imaged in reflection-seismic data at a variety of depths and under a variety of overburden conditions. This is important because sill-complexes present significant challenges for seismic interpretation, seismic processing, geologic forecasting and drilling. This has been investigated by generating synthetic seismograms using a 2D convolution method on a seismic-scale, sill-bearing outcrop-section from east Greenland, performing ray-based modelling to investigate lateral resolution at target depth for a variety of overburdens and target depths, and by comparing the synthetic seismograms to actual seismic. The main findings are:

1) It is important to be aware of the illumination at the target depth, as poor illumination leads to low maximum imaged dips and low lateral resolution. This will make it impossible to image steeply dipping features such as oblique dykes which might have important reservoir implications. 1D seismic convolution does not take

horizontal resolution into account, and consistently overestimates horizontal resolution.

2) Igneous rocks, such as basalt flows or shallow mafic intrusions, occurring between the imaging target and the seismic source and receivers will decrease vertical and particularly horizontal resolution at the target depth by absorbing high frequencies, seismic energy and diverting low-incidence seismic rays.

3) Commonly used rules-of-thumb for seismic detectability likely underestimate the minimum thickness of beds of mafic intrusions that may be imaged in reflection seismic data because of the high acoustic impedance contrast between mafic intrusions and siliciclastic rocks.

4) The thickness of sills, either thick or thin, is no guarantee that they might be imaged. Migrated seismic data has the potential to image thin sills if the velocity models are good and sills are not so close that they interfere with each other.

5) In reflection-seismic data of a reasonable quality, subseismic sill emplacement features such as splays, broken bridges and transgressive dykes may be inferred from sill geometries and amplitude variations.

6) Apparent steps (pseudosteps) in on sills imaged in seismic data arising from interference between a layered host-rock and oblique dykes is likely not to occur in actual seismic data at greater depths (> 1.5-2 km) because of limited horizontal resolution.

7) Improved imaging of sill-complexes is important and may be achieved by integrating conceptual understanding of sill-complexes and improved velocity models. We hope this paper may act as a starting point for discussion of the solutions to 'Sub-Sill Imaging'.

9. Acknowledgements

10. References

Ahokas, J.M., Nystuen, J.P., and Martinius, A.W., (2014a) Depositional dynamics and sequence development of the paralic Early Jurassic Neill Klinter Group, Jameson Land Basin, East Greenland: Comparison with the Halten Terrace, mid-Norwegian continental shelf. In: From depositional systems to sedimentary successions on the Norwegian Continental Shelf (Eds A. W. Martinius, R. Ravnås, J. A. Howell, R. J. Steel, and J. P. Wonham), Int. Assoc. Sedimentol. Spec. Publ. 46, 291-333.

Amante, C. and B.W. Eakins, 2009. ETOPO1 1 Arc-Minute Global Relief Model: Procedures, Data Sources and Analysis. NOAA Technical Memorandum NESDIS NGDC-24. National Geophysical Data Center, NOAA. doi:10.7289/V5C8276M

Baig, I., Faleide, J. I., Jahren, J., & Mondol, N. H. (2016). Cenozoic exhumation on the southwestern Barents Shelf: Estimates and uncertainties constrained from compaction and thermal maturity analyses. Marine and Petroleum Geology, 73, 105-130.

Brooks, C.K., (1973). Rifting and doming in southern East Greenland. Nat. Phys. Sci. 244, 23–24.

Brooks, C. K. (2011). The East Greenland rifted volcanic margin. Geological Survey of Denmark and Greenland Bulletin, 24, 96.

Brown, A. R. (2011). Interpretation of three-dimensional seismic data. Society of Exploration Geophysicists and American Association of Petroleum Geologists.

Bryan, S. E., & Ferrari, L. (2013). Large igneous provinces and silicic large igneous provinces: Progress in our understanding over the last 25 years. Geological Society of America Bulletin, 125(7-8), 1053-1078.

Buckley, S.J., Vallet, J., Braathen, A. and Wheeler, W. (2008) Oblique helicopter-based laser scanning for digital terrain modelling and visualization of geological outcrops. Int Arch Photogrammetry, Remote Sens Spatial Inform Sci, 37, 493–498.

Cartwright, J and Hansen, D.M. (2006) Magma transport through the crust via interconnected sill complexes. Geology, 31, 929-932.

Cartwright, J., & Huuse, M. (2005). 3D seismic technology: the geological 'Hubble'. Basin Research, 17, 1-20.

Cukur, D., Horozal, S., Kim, D. C., Lee, G. H., Han, H. C., & Kang, M. H. (2010). The distribution and characteristics of the igneous complexes in the northern East China Sea Shelf Basin and their implications for hydrocarbon potential. Marine Geophysical Researches, 31(4), 299-313.

Dam, G. and Surlyk, F. (1998) Stratigraphy of the Neill Klinter Group; a Lower – lower Middle Jurassic tidal embayment succession, Jameson Land, East Greenland. Geology of Greenland Survey Bulletin, 175, 80 pp.

Eide, C. H., Howell, J. A., Buckley, S. J., Martinius, A. W., Oftedal, B. T., & Henstra, G. A. (2016). Facies model for a coarse-grained, tide-influenced delta: Gule Horn Formation (Early Jurassic), Jameson Land, Greenland. Sedimentology, 63(6), 1474-1506.

Eide, C. H., Schofield, N., Jerram, D. A., & Howell, J. A. (2017). Basin-scale architecture of deeply emplaced sill complexes: Jameson Land, East Greenland. Journal of the Geological Society, 174(1), 23-40.

Eldhom, O., & Coffin, M. F. (2000). Large igneous provinces and plate tectonics. The history and dynamics of global plate motions, 309-326.

Faleide, J. I., Tsikalas, F., Breivik, A. J., Mjelde, R., Ritzmann, O., Engen, O., Wilson, J., & Eldholm, O. (2008). Structure and evolution of the continental margin off Norway and the Barents Sea. Episodes, 31(1), 82-91.

Fernandes, K. (2011). Irish sills of the North Atlantic Igneous Province: seismic imaging, observations and implications for climate change. Unpublished PhD Thesis, University of Dublin, Trinity College. 347 pp.

Flecha, I., Carbonell, R., Hobbs, R. W., & Zeyen, H. (2011). Some improvements in subbasalt imaging using pre-stack depth migration. Solid Earth, 2(1), 1.

Fliedner, M.M. and White, R.S., 2003. Depth imaging of basalt flows in the Faeroe–Shetland Basin. Geophysical Journal International, 152, 353-371.

Gallagher, J. W., & Dromgoole, P. W. (2007). Exploring below the basalt, offshore Faroes: a case history of sub-basalt imaging. Petroleum Geoscience, 13(3), 213-225.

Galland, O. (2012). Experimental modelling of ground deformation associated with shallow magma intrusions. Earth and Planetary Science Letters, 317, 145-156.

Galland, O., Planke, S., Neumann, E.-R., Malthe-Sørenssen, A. (2009) Experimental modelling of shallow magma emplacement: Application to saucer-shaped intrusions. Earth Planet. Sci. Lett., 277, 373-383.

Gilbert, G.K., 1877. Report on the Geology of the Henry Mountains. US Government Printing Office. 160 pp.

Gjøystdal, H., Iversen, E., Lecomte, I., Kaschwich, T., Drottning, Å., & Mispel, J. (2007). Improved applicability of ray tracing in seismic acquisition, imaging, and interpretation. Geophysics, 72(5), SM261-SM271.

Gray, S.H., Etgen, J., Dellinger, J. and Whitmore, D., 2001. Seismic migration problems and solutions. Geophysics, 66, 1622-1640.

Hafeez, A., Planke, S., Jerram, D. A., Millett, J. M., Maharjan, D., & Prestvik, T. (2017). Upper Paleocene ultramafic igneous rocks offshore mid-Norway: Reinterpretation of the Vestbrona Formation as a sill complex. Interpretation, 5(3), SK103-SK120.

Hald, N. and Tegner, C. (2000) Composition and age of tertiary sills and dykes, Jameson Land Basin, East Greenland: relation to regional flood volcanism. Lithos, 54, 207-233.

Hansen D.M. and Cartwright, J. (2006a). Saucer-shaped sill with lobate morphology revealed by 3D seismic data: implications for resolving a shallow-level sill mechanism. J. Geol. Soc. London, 163, 509-523.

Hansen, D. M., & Cartwright, J. (2006b). The three-dimensional geometry and growth of forced folds above saucer-shaped igneous sills. Journal of Structural Geology, 28(8), 1520-1535.

Hanssen, P., Ziolkowski, A. and Li, X.Y., 2003. A quantitative study on the use of converted waves for sub-basalt imaging. Geophysical Prospecting, 51, 183-193.

Hardy, R., Bednar, J.B., Bednar, C., Fernandes, K. and Jones, S.M., 2008, June. Imaging Beneath Igneous Sills Using Reverse Time Depth Migration. In 70th EAGE Conference and Exhibition incorporating SPE EUROPEC 2008.

Henriksen, E., Bjørnseth, H. M., Hals, T. K., Heide, T., Kiryukhina, T., Kløvjan, O. S., Larssen, G. B., Ryseth, A. E., Rønning, K., Sollid, K & Stoupakova, A. (2011). Uplift and erosion of the

greater Barents Sea: impact on prospectivity and petroleum systems. Geological Society, London, Memoirs, 35(1), 271-281.

Hersum, T.G., Marsh, B.D., and Simon A.C. (2007). Contact Partial Melting of Granitic Country Rock, Melt Segregation, and Re-injection as Dikes into Ferrar Dolerite Sills, McMurdo Dry Valleys, Antarctica. J. Petrology (2007) 48 (11): 2125-2148.

Holford, S., Schofield, N., MacDonald, J., Duddy, I., & Green, P. (2012). Seismic analysis of igneous systems in sedimentary basins and their impacts on hydrocarbon prospectivity: Examples from the southern Australian margin. The APPEA Journal, 52(1), 229-252.

Hunt, C.B., Averitt, P. and Miller, R.L., 1953. Geology and geography of the Henry Mountains region, Utah (No. 228). US Government Printing Office. 244 pp.Hutton, D.H.W. (2009) Insights into magmatism in volcanic margins: bridge structures and a new mechanism of basic sill emplacement - Theron Mountains, Antartica. Petroleum Geoscience, 15, 269-278.

Ichaso, A.A. and Dalrymple, R.W. (2014) Eustatic, tectonic and climatic controls on an early syn-rift mixed-energy delta, Tilje Formation (Early Jurassic, Smørbukk field, offshore mid-Norway). In: From Depositional Systems to Sedimentary Successions on the Norwegian Continental Margin (Eds A. W. Brooks, R. Ravnås, J. A. Howell, R. J. Steel and P. Wonham), IAS Spec. Publ 46, 339-388.

Jackson, C. A., Schofield, N., & Golenkov, B. (2013). Geometry and controls on the development of igneous sill–related forced folds: A 2-D seismic reflection case study from offshore southern Australia. Geological Society of America Bulletin, 125(11-12), 1874-1890.

Jerram, D.A. & Bryan, S. E. 2015. Plumbing Systems of Shallow Level Intrusive Complexes. Part of the series Advances in Volcanology pp 1-22, Springer.

Jerram, D.A., Davis, G.R., Mock, A., Charrier, A., and Marsh, B.D. (2010). Quantifying 3D crystal populations, packing and layering in shallow intrusions: a case study from the Basement Sill, Dry Valleys, Antarctica. GEOSPHERE Volume: 6 Issue: 5 Pages: 5

Johnson, A.M. and Pollard, D.D., 1973. Mechanics of growth of some laccolithic intrusions in the Henry mountains, Utah, I: field observations, Gilbert's model, physical properties and flow of the magma. Tectonophysics, 18, pp.261-309.

Kallweit, R. S., & Wood, L. C. (1982). The limits of resolution of zero-phase wavelets. Geophysics, 47(7), 1035-1046.

Lecomte, I., Lavadera, P. L., Botter, C., Anell, I., Buckley, S. J., Eide, C. H., Grippa, A., Mascolo, V. and Kjoberg, S. (2016). 2 (3) D convolution modelling of complex geological targets beyond 1D convolution. First Break, 34, 99-107.

Lecomte, I., Lavadera, P. L., Anell, I., Buckley, S. J., Schmid, D. W., & Heeremans, M. (2015). Ray-based seismic modeling of geologic models: Understanding and analyzing seismic images efficiently. Interpretation, 3(4), SAC71-SAC89.

Magee, C., Jackson, C. L., & Schofield, N. (2014). Diachronous sub-volcanic intrusion along deep-water margins: Insights from the Irish Rockall Basin. *Basin Research*, *26*(1), 85-105.

Magee, C., Hunt-Stewart, E., & Jackson, C. A. L. (2013). Volcano growth mechanisms and the role of sub-volcanic intrusions: Insights from 2D seismic reflection data. Earth and Planetary Science Letters, 373, 41-53.

Magee, C., Maharaj, S. M., Wrona, T., & Jackson, C. A. L. (2015). Controls on the expression of igneous intrusions in seismic reflection data. Geosphere, 11, 1024-1041.

Magee, C., Muirhead, J.D., Karvelas, A., Holford, S.P., Jackson, C.A.L, Bastow, I. D., Schofield, N., Stevenson, C.T.E., McLean, C., McCharty, W., and Shtukert, O. (2016). Lateral magma flow in mafic sill complexes. Geosphere, 12(3), 809-841.

Larsen, H.C. and Marcussen, C. (1992) Sill-intrusion, flood basalt emplacement and deep crustal structure of the Scoresby Sund Region, East Greenland. In: Magmatism and the Causes of Continental Break-up (Eds B.C. Storey, T. Alabaster and R.J. Pankhurst), Geological Society Special Publication, 68, 365-368.

Martinius, A.W., Kaas, I., Næss, A., Helgesen, G, Kjærefjord, J.M. and Leith, D.A. (2001) Sedimentology of the heterolithic and tide-dominated Tilje Formation (Early Jurassic, Halten Terracce, offshore mid-Norway). In: Sedimentary Environments Offshore Norway - Palaeozoic to Recent (Eds O. J. Martinsen and T. Dreyer) NPF Special Publication 10, 103-144.

Mathiesen, A., Bidstrup, T., Christiansen, F.G. (2000) Denudation and uplift history of the Jameson Land basin, East Greenland - constrained from maturity and apaite fission track data. Global and Planetary Change, 24, 275-301.

Millett, J. M., Wilkins, A. D., Campbell, E., Hole, M. J., Taylor, R. A., Healy, D., Jerram, D. A., Jolley, D. W., Planke, S., Archer, S. G., & Blischke, A. (2016). The geology of offshore drilling through basalt sequences: Understanding operational complications to improve efficiency. Marine and Petroleum Geology, 77, 1177-1192.

Minakov, A., Yarushina, V., Faleide, J. I., Krupnova, N., Sakoulina, T., Dergunov, N., & Glebovsky, V. (2017). Dyke emplacement and crustal structure within a continental large igneous province, northern Barents Sea. Geological Society, London, Special Publications, 460, SP460-4.

Muirhead, J. D., Airoldi, G., White, J. D., & Rowland, J. V. (2014). Cracking the lid: Sill-fed dikes are the likely feeders of flood basalt eruptions. *Earth and Planetary Science Letters*, *406*, 187-197.

Muirhead, J. D., Van Eaton, A. R., Re, G., White, J. D., & Ort, M. H. (2016). Monogenetic volcanoes fed by interconnected dikes and sills in the Hopi Buttes volcanic field, Navajo Nation, USA. Bulletin of Volcanology, 78(2), 1-16.

Muirhead, D.K., Bowden, S.A., Parnell, J. & Schofield, N. *(in press)*. Muirhead, Source rock maturation owing to igneous intrusion in rifted margin petroleum systems. Journal of the Geological Society

O'Brien, P.N.S. and Lucas, A.L., 1971. Velocity dispersion of seismic waves. *Geophysical Prospecting, 19*, 1-26.

Omosanya, K. O., Johansen, S. E., & Abrahamson, P. (2016). Magmatic activity during the breakup of Greenland-Eurasia and fluid-flow in Stappen High, SW Barents Sea. Marine and Petroleum Geology, 76, 397-411.

Planke, S., Rasmussen, T., Rey, S.S., and Myklebus, R. (2005) Seismic characteristics and distribution of volcanic intrusions and hydrothermal vent complexes in the Vøring and Møre basins. In: Petroleum Geology: North-West Europe and Global Perspectives—Proceedings of the 6th Petroleum Geology Conference (Eds A. G. Dore and B. A. Vining), 833-844.

Planke, S., Svensen, H., Myklebust, R., Bannister, S., Manton, B. & Lorenz, L. 2015. Geophysics and Remote Sensing. In: Breitkreuz, C. & Rocchi, S. (eds.) Advances in Volcanology. Springer Berlin, Heidelberg, 1-16.

Purnell, G.W., 1992. Imaging beneath a high-velocity layer using converted waves. Geophysics, 57, 1444-1452.

Rateau, R., Schofield, N., & Smith, M. (2013). The potential role of igneous intrusions on hydrocarbon migration, West of Shetland. Petroleum Geoscience, 19(3), 259-272.

Rittersbacher, A., Buckley, S. J., Howell, J. A., Hampson, G. J. and Vallet J. (2013) Helicopter-based laser scanning: a method for quantitative analysis of large-scale sedimentary architecture. In: Sediment-Body Geometry and Heterogeneity: Analogue Studies for Modelling the Subsurface (Eds A. W. Martinius, J.A. Howell and T. Good), Geol. Soc. London Spec. Publ. 238

Rybach, L., & Buntebarth, G. (1984). The variation of heat generation, density and seismic velocity with rock type in the continental lithosphere. Tectonophysics, 103(1-4), 335-344.

Saunders, A. D., Fitton, J. G., Kerr, A. C., Norry, M. J. and Kent, R. W. (1997). The North Atlantic Igneous Province. Geophysical Monograph 100, 45–93.

Scales, J. A., & Snieder, R. (1998). What is noise?. Geophysics, 63(4), 1122-1124.

Schmiedel, T., Kjoberg, S., Planke, S., Magee, C., Galland, O., Schofield, N., Jackson, C. A.-K., & Jerram, D. A. (2017). Mechanisms of overburden deformation associated with the emplacement of the Tulipan sill, mid-Norwegian margin. Interpretation, 5(3), SK23-SK38.

Schofield, N.J., Brown, D.J., Magee, C., and Stevenson, C.T. (2012a) Sill morphology and comparison of brittle and non-brittle emplacement mechanisms. J. Geol. Soc. 169, 127-141.

Schofield, N., Holford, S., Millett, J., Brown, D., Jolley, D., R Passey, S., Muirhead, D., Grove, C., Magee, C., Murray, J. and Hole, M., (2015). Regional magma plumbing and emplacement mechanisms of the Faroe-Shetland Sill Complex: implications for magma transport and petroleum systems within sedimentary basins. Basin Research.

Schofield, N., Jolley, D., Holford, S., Archer, S., Watson, D., Hartley, A., Howell, J., Muirhead, D., Underhill, J & Green, P. (2017). Challenges of future exploration within the UK Rockall

Basin. In Geological Society, London, Petroleum Geology Conference series (Vol. 8, pp. PGC8-37). Geological Society of London.

Schofield, N., Heaton, L., Holford, S.P, Archer, S.G., Jackson, C.A.-L and Jolley, D.W. (2012b) Seismic imaging of 'broken bridges': linking seismic to outcrop-scale investigations of intrusive magma lobes. J. Geol. Soc. London, 169, 421-426.

Schofield, N., Stevenson, C., and Reston, T. (2010) Magma fingers and host rock fluidization in the emplacement of sills. Geology, 38, 63-66.

Sclater, J.G. and Christie, P.A., (1980). Continental stretching: An explanation of the post-Mid-Cretaceous subsidence of the central North Sea Basin. Journal of Geophysical Research: Solid Earth, 85, 3711-3739.

Senger, K., Buckley, S. J., Chevallier, L., Fagereng, Å., Galland, O., Kurz, T. H., Ogata, K., Planke, S. & Tveranger, J. (2015). Fracturing of doleritic intrusions and associated contact zones: implications for fluid flow in volcanic basins. Journal of African Earth Sciences, 102, 70-85.

Senger, K., Millett, J., Planke, S., Ogata, K., Eide, C. H., Festøy, M., Galland, O., & Jerram, D. A. (2017) Effects of igneous intrusions on the petroleum system: a review. First Break, 35.

Sheriff, R. E. and Geldart, L. P. (1995). Exploration Seismology (2nd Edn). Cambridge University Press. 628 p.

Simm, R., & Bacon, M. (2014). Seismic Amplitude: An interpreter's handbook. Cambridge University Press.

Skogseid, J., Planke, S., Faleide, J. I., Pedersen, T., Eldholm, O., & Neverdal, F. (2000). NE Atlantic continental rifting and volcanic margin formation. Geological Society, London, Special Publications, 167(1), 295-326.

Smallwood, J. R., & Maresh, J. (2002). The properties, morphology and distribution of igneous sills: modelling, borehole data and 3D seismic from the Faroe-Shetland area. Geological Society, London, Special Publications, 197(1), 271-306.

Surlyk, F. (2003) The Jurassic of East Greenland: a sedimentary record of thermal subsidence, onset and culmination of rifting. In: The Jurassic of Denmark and Greenland (Eds.

J. R. Ineson and F. Surlyk), Geological Survey of Denmark and Greenland Bulletin, 1, p. 659-722.

Svensen, H., Polteau, S., Cawthorn, G., and Planke, S. (2015) Sub-volcanic intrusions in the Karoo Basin, South Africa. Advances in Volcanology. In Press. DOI: 10.1007/11157_2014_7

Talwani, M., & Eldholm, O. (1977). Evolution of the Norwegian-Greenland sea. Geological Society of America Bulletin, 88(7), 969-999.

Thomson, K. (2005) Volcanic features of the North Rockall Through: application of visualization techniques on 3D seismic reflection data. Bulletin of Volcanology, 67, 116-128.

Thomson, K., & Hutton, D. (2004). Geometry and growth of sill complexes: insights using 3D seismic from the North Rockall Trough. Bulletin of Volcanology, 66(4), 364-375.

Thomson, K., & Schofield, N. (2008). Lithological and structural controls on the emplacement and morphology of sills in sedimentary basins. Geological Society, London, Special Publications, 302(1), 31-44.

Vallet, J., & Skaloud, J. (2004). Development and experiences with a fully-digital handheld mapping system operated from a helicopter. The International Archives of the Photogrammetry, Remote Sensing and Spatial Information Sciences, Istanbul, 35 (Part B).

van Cappelle, M., Ravnås, R., Hampson, G. J., & Johnson, H. D. (2017). Depositional evolution of a progradational to aggradational, mixed-influenced deltaic succession: Jurassic Tofte and Ile formations, southern Halten Terrace, offshore Norway. Marine and Petroleum Geology, 80, 1-22.

Wall, M., Cartwright, J., Davies, R. and McGrandle, A., 2010. 3D seismic imaging of a Tertiary Dyke Swarm in the Southern North Sea, UK. Basin Research, 22, 181-194.

Walker, R. J., Healy, D., Kawanzaruwa, T. M., Wright, K. A., England, R. W., McCaffrey, K. J. W., Bubeck, A.A., Stephens, T.L., Farrell N.J.C & Blenkinsop, T. G. (2017). Igneous sills as a record of horizontal shortening: The San Rafael subvolcanic field, Utah. Geological Society of America Bulletin.

Widess, M.B. 1973. How thin Is a thin bed? Geophysics, 38, 1176-1180.

Ziolkowski, A., Hanssen, P., Gatliff, R., Jakubowicz, Li, X.-Y., Jakubowicz, H & Hampson, G. (2003). Use of low frequencies for sub-basalt imaging. Geophysical Prospecting, 51(3), 169-182.

12. Tables

Table 1: Input data for modeling. NCS, Norwegian Continental Shelf; MD, measured depth, FA; Facies association.

a) Values for target at 1 and 3 km depth

Name	Facies association #	V_P km/s	V_P/V_S fraction	Density g/cm3	Source NCS well/article	Depth MD (m)
Igneous intrusions	1	6.3	1.86	3.0	Smallwood and Maresh, 2002	
Homogeneous sandstone	2	3.7	1.80	2.5	Add 5% to FA3	-
Sandstone	3	3.5	1.80	2.4	6407/2-1	3220-3235
Poorly cemented sandstone	4	3.4	1.80	2.3	Subtract 5% from FA3	-
Heterolithic	5	3.3	1.80	2.3	6407/2-1	3030-3050
Mudstone	6	3.8	1.80	2.5	6407/2-1	2920-2940
Organic rich mudstone	7	2.6	1.80	2.3	6407/2-1	2885-2900

b) Values for target at 6 km depth

Name	Facies association #	V_P km/s	V_P/V_S fraction	Density g/cm3	Source NCS well/article	Depth MD (m)
Igneous intrusions	1	6.3	1.86	3.0	Smallwood and Maresh, 2002	
Homogeneous sandstone	2	4.8	1.80	2.7	Add 5% to FA3	-
Sandstone	3	4.6	1.80	2.6	6506/12-10A	5525-5545m
Poorly cemented sandstone	4	4.4	1.80	2.4	Subtract 5% from FA3	-
Heterolithic	5	4.7	1.80	2.5	6506/12-10A	5565-5582m
Mudstone	6	4.7	1.80	2.4	6506/12-10A	5618-5635m
Organic rich mudstone	7	3.9	1.80	2.5	6506/12-10A	5330-5335m

13. Captions to supplementary files

A1: Input model to seismic modelling, presented in paper as Figure 5D. Extrapolated architectural model of the sill-bearing parts of the Hurry Inlet section. Each pixel is 3 m in horizontal extent and 0.5 m in vertical extent. The gray values correspont to the following facies associations (FA in Table 1): FA1 (igneous intrusions, 97), FA2 (homogeneous sandstone. 159), FA3 (Sandstone, 124), FA4 (Poorly cemented sandstone, 55), FA5 (Heterolithic, 130), FA6 (mudstone, 111), and FA7 (Organic rich mudstone, 0).

A2: Very high-resolution versions of panels on left side of Fig. 11, showing comments and synthetic seismograms overlain the outcrop model.

A3: Very high-resolution version of panels on right side of Fig. 11, showing A) outcrop; B) reflectivity model; C) synthetic seismogram generated with seismogram using a 40 Hz wavelet and 80° max dip; D) Synthetic seismogram generated with seismogram using a 20 Hz wavelet and 50° max dip; E) Synthetic seismogram generated with seismogram using a 15Hz wavelet and 30° max dip. F) Synthetic seismogram generated with seismogram using a 10 Hz wavelet and 30° max dip. PSF: Point-spread function.